

# Multistage dolomitization and fluid evolution of the late Ediacaran cap carbonates, Hormuz complex, Paskhand salt diapir, southern Iran: Insights into the dolomite problem

Sadegh Adineh<sup>a,b,\*</sup>, Prokop Závada<sup>b</sup>, Soumyajit Mukherjee<sup>c</sup>, Jiří Bruthans<sup>a</sup>, Mohammad Zare<sup>d</sup>

<sup>a</sup> Faculty of Science, Charles University in Prague, Albertov 6, 128 43 Praha 2, Czech Republic

<sup>b</sup> Institute of Geophysics ASCR, Boční II 1a/1401, Prague, Czech Republic

<sup>c</sup> Department of Earth Sciences, Indian Institute of Technology Bombay, Powai, Mumbai 400 076, Maharashtra, India

<sup>d</sup> Department of Earth Sciences, College of Sciences, Shiraz University, 71454, Shiraz, Iran

## ARTICLE INFO

### Keywords:

Hormuz dolomite  
Hormuz complex  
Multiphase dolomitization  
Dolomitizing fluids  
Hydrothermal alteration

## ABSTRACT

The Late Ediacaran to early Cambrian Hormuz dolomites were originally deposited on a shallow marine platform within the southern proto-Tethys Ocean, undergoing significant dolomitization during this period. The origins of different types of dolomites and their original fluids were studied in this work through petrological, mineralogical and geochemical data, including carbon, oxygen and clumped isotopes. The laminated micritic dolomite (LMD) (very finely to finely crystalline planar-e/s dolomite with preserving fabrics) and matrix dolomite (MD) including D1 (very finely to finely crystalline planar-e/s dolomite), the D2 (finely to medium crystalline planar-s/a dolomite) and D3 (medium to coarsely crystalline nonplanar-a dolomite) were precipitated from the combination of hydrothermal fluids and hydrologically cycled seawater in the subsurface to shallow burial stage. Fluctuation of the temperatures and changes in the characteristics of dolomitizing fluids formed different textures and distributions in the dolomites. Due to changes in temperature and  $Mg^{2+}$  concentrations in the hydrothermal fluids, the precipitation of cemented dolomite (CD1) and cemented dolomite (CD2 or SD) exhibited different textures and filling fracture system. In the final phase of hydrothermal alteration, late-stage calcite precipitates at low temperatures as a result of decreasing  $Mg^{2+}$  concentrations. Hydrothermal fluids, depleted in  $Mg^{2+}$  and enriched in silica, could result from the dissolution of siliciclastic sediments. The silica could be sourced from igneous rocks driven by the strongly extensional faults in the back-arc in Cadomian margin during the late Ediacaran time. The isotopic and petrographic analysis of the dolostones within the caprock of the Paskhand salt diapir indicate that their dolomitization occurred under hydrothermal and shallow burial conditions within the extensional back-arc Hormuz basin during late Ediacaran time. Dolomites exhibiting negative  $\delta^{13}C$  values in the cap rock of the Paskhand salt diapir likely formed during the late Ediacaran period. This isotopic signature suggests that hydrothermal fluids interacted with organic-rich sediments, incorporating isotopically light carbon into the dolomite structure. This study provides new insights into the evolution of dolomitizing fluids responsible for multiple dolomitization events and the formation of hydrothermal dolomite in the Hormuz Basin and other regions worldwide.

## 1. Introduction

Dolomite (calcium magnesium carbonate -  $CaMg(CO_3)_2$ ) is one of the most common minerals in the Ediacaran marine successions (Wang et al., 2023a,b). However, dolomite is less common in the modern sedimentary environments. This paradox has been studied for decades without any clear explanation known as the “dolomite problem” (e.g.,

Holland and Zimmermann, 2000; Warren, 2000; McKenzie and Vasconcelos, 2009; Gregg et al., 2015). Rare existing dolomite in modern shallow environments is due to the challenges associated with its precipitation under typical Earth-surface conditions. In natural setting, these challenges arise from hydration effects that make it more difficult for  $Mg^{2+}$  to be incorporated into the dolomite crystal structure than to calcite. Additionally, these effects can hinder the bonding of  $Mg^{2+}$  with

\* Corresponding author. Faculty of Science, Charles University in Prague, Albertov 6, 128 43 Praha 2, Czech Republic.

E-mail addresses: [s.adineh@ig.cas.cz](mailto:s.adineh@ig.cas.cz), [sadeghadineh7@gmail.com](mailto:sadeghadineh7@gmail.com) (S. Adineh).

<https://doi.org/10.1016/j.marpetgeo.2024.107228>

Received 19 September 2024; Received in revised form 22 November 2024; Accepted 25 November 2024

Available online 27 November 2024

0264-8172/© 2024 Elsevier Ltd. All rights reserved, including those for text and data mining, AI training, and similar technologies.

$\text{CO}_3^{2-}$  in the boundary layer, which impedes crystal growth (Fang et al., 2023; Wang et al., 2023a,b). However, dolomite formation can occur in modern environments characterized by low-oxygen and low-sulfate conditions, which are linked to microbial activities (Warthmann et al., 2000; Liu et al., 2019). The frequency of dolomite in Precambrian marine successions is attributed to differences in geochemical environment and contemporaneous seawater composition —e.g., higher  $\text{Mg}^{2+}$  and lower sulfate concentrations, as well as variations in alkalinity, redox conditions and microbial activity compared to Phanerozoic seawater. These factors plausibly led dolomite to precipitate as a primary or early secondary mineral phase (Wood et al., 2017; Cantine et al., 2020; Chang et al., 2020).

Icehouse–greenhouse transition and post-glacier period led to the global deposition of cap carbonates (dolomites) during the Ediacaran Period (~635–539 Ma) (Wang et al., 2023a,b). These cap dolomites are distributed worldwide and are characterized by fine dolomites, giant ooids, tubestone stromatolites, tepee-like structures and barites (crystal fans) (Wang et al., 2023a,b). These got deposited through a series of petrological, sedimentological, biological, mineralogical and geochemical changes caused by the abrupt global warming that postdated the global glaciation (Hoffman, 2011). Thicknesses of these cap dolomites range few m and hundreds of m (Wang et al., 2023a,b). Over past decades, numerous studies mostly focused on the sedimentary facies interpretation and the formation models for the cap dolomites during the Ediacaran Period (Aftabi et al., 2022; Wang et al., 2023a,b). Notwithstanding, genesis of Ediacaran dolomites/dolomitization remains controversial. Significantly, the widely accepted hypothesis suggests burial–hydrothermal dolomitization of primary limestones ( $\text{CaCO}_3$ ) at  $> 100^\circ\text{C}$  plays a major role, which is supported by several petrographic observations (e.g., coarse dolomite cements, saddle dolomites) (model:  $2\text{CaCO}_3 + \text{Mg}^{2+} \rightarrow \text{CaMg}(\text{CO}_3)_2 + \text{Ca}^{2+}$  or  $\text{CaCO}_3 + \text{Mg}^{2+} + \text{CO}_3^{2-} \rightarrow \text{CaMg}(\text{CO}_3)_2$  (1)) (Bristow et al., 2011; Rooney et al., 2020). In contrast, other studies suggested dolomitization at lower temperatures ( $<60^\circ\text{C}$ ) where marine water was the dolomitizing fluid during the early diagenesis (model:  $\text{Ca}^{2+} + \text{Mg}^{2+} + 2\text{CO}_3^{2-} \rightarrow \text{CaMg}(\text{CO}_3)_2$  (2)) (Gregg et al., 2015). Given the limited formation of dolomite in modern surface environments, direct evidence for the formation of early diagenetic dolomites in the Precambrian likely underscores the significance of early formation pathways in the past.

Numerous salt diapirs are found in the Zagros Fold and Thrust Belt (ZFTB) within the Fars region (Fig. 1), sourcing from a thick sequence of Neoproterozoic to Early Cambrian carbonate-evaporite deposits known as the Hormuz Complex (Fig. 2) (e.g. Kent, 1958, 1979; Edgell, 1996; Mukherjee et al., 2010; Motamedi et al., 2011; Taghipour et al., 2013). Previous studies on the Hormuz carbonates in few salt diapirs (e.g., Hormuz Island and Paskahnd salt diapir) revealed that the host rock predominantly consist of syn/post glaciogenic dolomitic diamictite-cap carbonate successions (e.g., Aftabi et al., 2022; Adineh et al., 2023). The existence of *Spriggina* discs and genus *Collenia* in the Hormuz dolomitic cap carbonates, shaly carbonates (Kent, 1979; Aftabi et al., 2022) and U-Pb zircon dating of  $558 \pm 7$  Ma on fresh rhyolites (Faramarzi et al., 2015) confirmed late Ediacaran age for dolomitic successions associated with Iranian salt diapirs in southern Iran. Paskhand salt diapir is one of these limited unroofed salt diapirs, which is associated with late Ediacaran syn/post glacial deposits—such as diamictite, cap carbonate, and dolomitic stromatolite (Adineh et al., 2023). These dimictite-cap carbonate successions should be studied with special attention on the origin and mechanism of the dolomite formation.

The characteristics of late Ediacaran carbonate clasts associated with Paskhand salt diapir provide new insight into mechanism of dolomite formation in the enigmatic cap carbonate formation during late Ediacaran time. In this article, detailed meso- and microscopic petrographic studies, isotope geochemistry of oxygen and carbon, and carbonate clumped-isotope ( $\Delta_{47}$ ) paleo temperature ( $T_{\Delta 47}$ ) record were conducted on cap carbonate samples brought from 8 to 10 km depth by diapirism in the Paskhand salt diapir from the late Ediacaran Hormuz Complex in

southern Iran. All in all, our main objectives thus comprise of the following: (i) examine the variations in petrographic and geochemical characteristics of Late Ediacaran-Early Cambrian dolomites; (ii) study the factors influencing the formation and distribution of these dolomites and their distinct characters, and (iii) determine the geochemical characteristics of the fluids responsible for dolomitization, thereby constraining their genesis.

Salt diapirs in the Persian Gulf serve as effective seal or cap rocks for hydrocarbon reservoirs (e.g., ME Asl et al., 2019; Faghieh et al., 2019). Dolomite facies, which often function as reservoir rocks, have recently gained attention in petroleum geology, with studies conducted in various regions worldwide (e.g., Braithwaite et al., 2004; Gregg et al., 2004). In this context, the Paskhand salt diapir is of particular geo-scientific interest, and this article aims to explore it in detail.

## 2. Geology

The Zagros Fold and Thrust Belt is located, from a global tectonic point of view, in the northern part of the Arabian plate, which is tilted in the northwest (Thomas et al., 2015). The Zagros Fold and Thrust Belt comprises Precambrian basement rocks, extensively covered by up to 10 km of late Neoproterozoic to Phanerozoic sedimentary rocks (Adineh et al., 2024). The basement of the Arabian Plate is largely unknown due to the lack of outcrops, except in some areas of Oman. The Arabian Plate has been reviewed by Stern and Johnson (2010). The oldest rocks are limited to the small inlier of Mirbat in southern coastal Oman (Mercolli et al., 2006). In this outcrop, the crystalline basement is covered unconformably by a thick sequence of Cryogenian to Ediacaran volcano-sedimentary rocks, containing glaciogenic sedimentary succession—such as diamictites (Allen, 2007). These glacial deposits were identified in two main phases of depositions, which may correlate with the Sturtian and Marinoan global Earth snowball events (Bowring et al., 2007). These volcano sedimentary deposits known as Huqf Supergroup were precipitated in the extensional grabens with orientated N–S in present day coordinates (Allen, 2007). The Huqf Supergroup continued depositing into the Cambrian, with the Cambrian-Precambrian boundary within the lower part of the Ara Group (equivalent to the Hormuz Salt). Smith (2012) reviews its distribution and evolution of the Huqf Supergroup. The sedimentation of the Ara-Hormuz deposits was locally associated with contemporaneous volcanism (Ramezani and Tucker, 2003; Allen, 2007; Faramarzi et al., 2015; Asadi Sarshar et al., 2022). The contemporaneous igneous activity is interpreted as resulting from the subduction of proto-Tethyan crust beneath the continental margin, transforming the Oman region into a retro-arc setting on the northeastern Arabian margin (Ramezani and Tucker, 2003; Faramarzi et al., 2015). Thick carbonate-evaporite successions were deposited in number of minibasins in the Zagros Fold and Thrust belt (Bahroudi and Koyi, 2003). It is clear that due to the lack of outcropping late Ediacaran carbonates and the presence of a thick cover, only those rocks brought up by unroofed salt diapirs, which are the focus of our study, are accessible for detail examination.

### 2.1. Paskhand salt diapir

Salt diapirs are associated with various forms of dolomitization (Table 1). However, the dolomites linked to Iranian salt diapirs are particularly unique because they originate from late Ediacaran Hormuz dolomites. Salt diapirs of varying sizes are exposed in the Zagros Fold-Thrust Belt (ZFTB) in southern Iran (Fig. 1A). The Paskhand salt diapir (Fig. 1B), with an elliptical outcrop measuring ~2.5 km east-west and ~1.5 km north-south, is one of the smallest emergent salt diapirs in the ZFTB. It is particularly notable for uniquely preserving the sedimentary characteristics of late Ediacaran depositions, which is observed as megaclast ( $>3$  m) at the surface of the unroofed diapir. These megaclasts are mostly heterogeneous in terms of grain size, clast content, alteration mineralogy, internal structures and fabrics (Fig. 3). Most

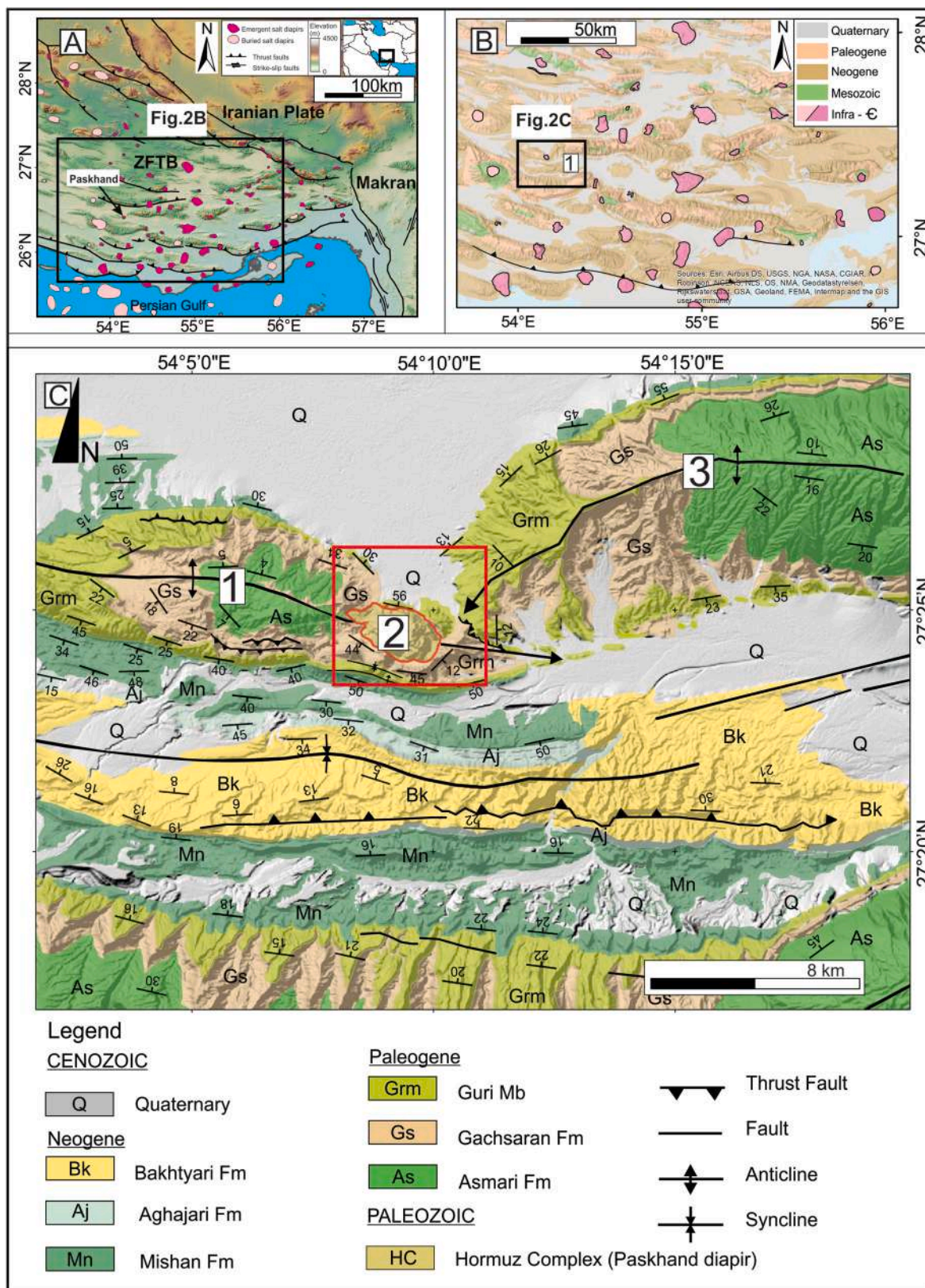


**Fig. 1.** A. Regional structural map of the Zagros Fold and Thrust Belt (ZFTB), depicting major structural elements such as the Zagros Fold and Thrust Belt, the Iranian plate, and the Makran zone (modified from Adineh et al., 2024). B. Geological map of the coastal Fars region, showing the distribution of exposed and hidden salt structures (modified from Závada et al., 2021; Adineh et al., 2024). Number correspond to studied salt diapir: 1 - Paskhand salt diapir (Bosák et al., 1998; Jahani et al., 2007). C. Simplified geological map of the study area overlaid with ASTER GDEM data. The study area is highlighted by a red square, corresponding to the black rectangle in Fig. 2B. Key features are numbered: 1 - Paskhand Anticline, 2 - Paskhand salt diapir, 3 - Siah Tagh Anticline (modified from Adineh et al., 2024). The geological map is adapted from Farzipour Saenen et al. (2007). Coordinates are given in UTM Zone 41N, WGS 84. For color interpretation, refer to the web version of the article.

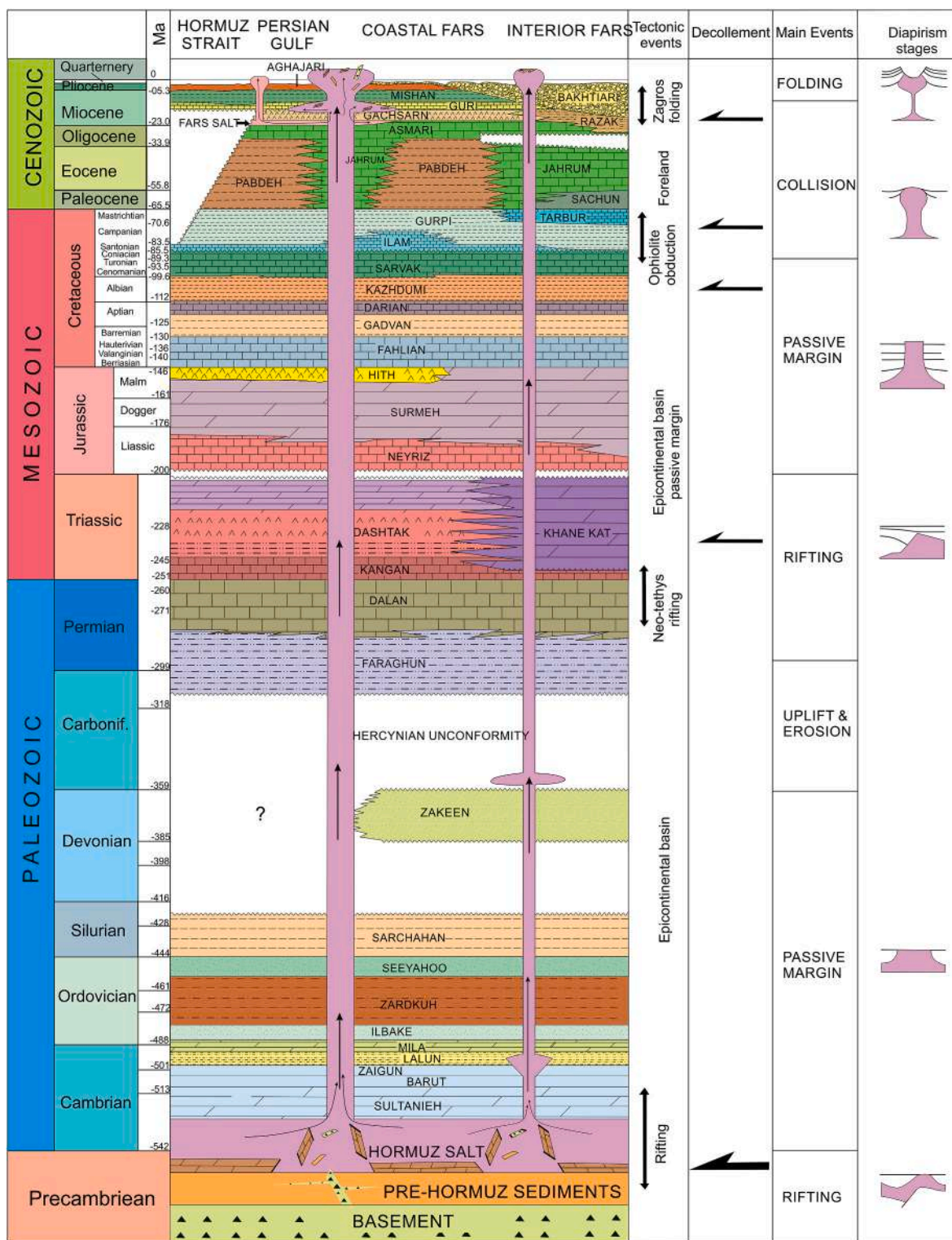


Fig. 2. Stratigraphic column of the central and eastern Zagros Fold and Thrust Belt (modified after Závada et al., 2021; Adineh et al., 2023).

sedimentary outcrops feature clasts of  $\geq 3$  m in size, and they are notably well-preserved, retaining the distinct characteristics of the sedimentary layers (Fig. 3). Table 2 presents various types of sedimentary lithotypes along with interpretations of their respective depositional environments (detail in Adineh et al., 2023). However, this study is only focused on the late Ediacaran cap carbonates, which is overlain on the dolomitic diamictites (Fig. 3). The late Ediacaran cap carbonate of the Hormuz Complex, located within the Paskhand salt diapir, is distinguished by

several unique sedimentary features. These include tepee-like structures and sheet cracks (Fig. 4A), with 1–10 cm thick layers. The layers display a color spectrum from light grey to black and light brown. This unit is also associated with oolitic dolostone and stromatolitic dolostone (Fig. 4B–D). The stromatolitic dolostone is further divided into domal and laminated/wavy stromatolitic dolomites (Fig. 4C and D). In some instances, the cap carbonate is marked by red and black dolomite veins (Fig. 4E). Additionally, quartz and calcite veins are observed in the

**Table 1**  
Characteristics of dolomites associated with salt diapirs around the world.

No.	Author(s)	Terrain & Country	Approaches	Keys conclusion
1	<a href="#">Kent (1979)</a>	Dolostone in seven salt diapirs, in southern Iran and Persian Gulf	Field observations	Presence of Spriggina discs, and the genus <i>Collenia</i> in the Hormuz dolomitic cap carbonates and shaly carbonates indicate an Ediacaran age for the glaciogenic iron ores in the Hormuz Formation. The origin of laminated dolomite is stromatolite.
2	<a href="#">Posey et al. (1987)</a>	Carbonate caprock in seven salt diapirs located in the East Texas Basin, North Louisiana Basin, Mississippi Basin, and Gulf Coast Basin in USA	Petrographic analysis; Sr and S isotope analyses	Carbonate caprocks associated with salt diapirs formed through multiple biochemical stages involving dissolution and precipitation. These processes were influenced by various fluid types temporally, including marine waters, formation waters and low-salinity meteoric water. Episodic hydrocarbon migration played an important role in the evolution of the carbonate caprock.
3	<a href="#">Al-Aasm and Hassen (2006)</a>	dolomite in salt diapirs in central Tunisia	Field observations; petrography (light microscopy and cathodoluminescence); fluid inclusions; geochemical analysis (stable oxygen and carbon isotopes, strontium isotopes)	Dolomites were classified based on coloring including white and black. White dolomites have narrow ranges of $\delta^{18}\text{O}$ and $\delta^{13}\text{C}$ values ( $-3.83\text{‰}$ to $-6.60\text{‰}$ VPDB for $\delta^{18}\text{O}$ ; $-2.11\text{‰}$ to $-2.83\text{‰}$ VPDB for $\delta^{13}\text{C}$ values), while black dolomites show wider ranges and more depleted values ( $-4.92\text{‰}$ to $-9.97\text{‰}$ for $\delta^{18}\text{O}$ ; $-0.55\text{‰}$ to $-6.08\text{‰}$ for $\delta^{13}\text{C}$ values. Most samples have $^{87}\text{Sr}/^{86}\text{Sr}$ ratios near Triassic seawater values, indicating a primary source from Triassic saliferous rocks. Dolomitization involved at least two different fluids. The main fluid was deep hydrothermal or basinal, (related to the Triassic saliferous rocks) that ascended through faults during diapirism. A secondary less significant fluid source was meteoric water from the Cretaceous rocks.
4	<a href="#">Nasir et al. (2008)</a>	Geology and petrology of the Hormuz dolomite, Halul and Shraouh islanls, Persian Gulf	Field, petrographic, mineralogic and geochemical analyses	Dolomites formed in a reducing environment, presumably intertidal to supratidal settings, as indicated by stromatolitic structures and the presence of organic matter. Two dolomitization models were supported: a sabkha model and an organogenic model involving microbial activity. The Sr isotopic ratios were abnormally high, suggesting an addition of radiogenic Sr from a continental source or the salt-rich Hormuz Formation. Dolomite extensively recrystallized and sulfatized during salt doming. The presence of organic materials and high correlation of Si, Al, Ti, Zr, and insoluble residue suggest detrital minerals like quartz, rutile, and zircon were present, pointing to a sabkha setting and brine reflux related dolomitization.
5	<a href="#">Ghazban and Al-Aasm (2010)</a>	Dolostone in the Hormuz Island, Hormuz Complex, southern Iran	Field observations, petrographic studies (light microscopy and cathodoluminescence); fluid inclusions, geochemical analysis (stable oxygen and carbon isotopes, strontium, and sulfur isotopes)	Dolomites were classified based on coloring (white and black). $\delta^{13}\text{C}$ values indicate different carbon sources, with black dolomites ( $-0.81$ to $-2.07\text{‰}$ ) showing contributions from seawater bicarbonates and white/grey dolomites ( $-17.81$ to $-35.68\text{‰}$ VPDB) indicating significant contributions from hydrocarbon oxidation. Sea water is the main source of carbon and Mg for dolomite precipitation. The temperature of dolomite formation, determined from fluid inclusions, ranged from 213 to 216 °C. Pyrites and native sulphurs associated with the dolomites have $\delta^{34}\text{S}$ values ranging from $+17.2$ to $+23.4\text{‰}$ , indicating thermochemical sulfate reduction as the primary source of sulfur.

(continued on next page)

Table 1 (continued)

No.	Author(s)	Terrain & Country	Approaches	Keys conclusion
6	Thomas et al. (2015)	Dolostone in eight salt diapirs, Hormuz Complex, Persian Gulf	Field observations	Low-grade metamorphosed heavily recrystallized dolomites with randomly oriented plates of specular hematite.
7	Mortazavi et al. (2017)	Hydrothermal systems in dolomite associated with Gahkum salt diapir, southern Iran	Field observation, mineralogical studies	Observed mineral assemblages include calcite, apatite, garnet, epidote and hematite, formed as a result of hydrothermal interactions with host rocks. The presence of blue amphiboles (magnesian-riebeckite) in irregular veins and along fractures indicates significant hydrothermal fluid migration and alteration processes. The red or pink color of rocks and the occurrence of coarse euhedral hematite grains suggest migration of iron and manganese-rich hydrothermal fluids.
8	Perona et al. (2018)	Dolostones in the Murguía and Orduña saline diapirs in the Basque-Cantabrian Basin, Northern Spain	Field mapping, mineralogic and petrographic analysis, geochemical analysis (including sulfur, carbon and oxygen isotopes), fluid inclusion analysis, organic matter analysis	Thermal indicators (fluid inclusion, organic matter and sulfur isotope data) point to formation temperatures between 150 and 200 °C. The $\delta^{34}\text{S}$ values of sphalerite and galena (4.1–15.1‰) suggest a sulfur source related to the reduction of evaporite sulfate (thermochemical sulfate reduction) of Triassic age (15.3–17.4‰). The interaction of carbon-poor, metal- and sulfate-bearing hot brines with host rocks activated the cracking of organic matter, triggering sulfide precipitation at a rate controlled by $\text{H}_2\text{S}$ production. The $\delta^{13}\text{C}$ and $\delta^{18}\text{O}$ values of carbonates range from 3.5 to –20.5‰ and from 16.1 to 28.7‰, respectively, indicating different carbon sources and host-rock types. Sulfide deposits around the Murguía and Orduña salt domes are linked to the dolomitization of the surrounding rocks rather than the formation of caprock. This pattern is similar to the Mississippi Valley-type (MVT) deposits.
9	Poe et al. (2018)	Caprock assemblages in outcropping caprock from three different salt basins, Paradox Basin and Gulf Coast Region, USA and Flinders Ranges, South Australia	Facies mapping; petrographic analysis	Introducing new classification for the carbonate caprocks based on their fabrics. Massive fabric develops first in carbonate caprock formation. Porphyritic, layered and brecciated fabrics show a patchy distribution and are rarely correlative. Variations exist in caprock mineralogy between different localities. Episodes of hydrocarbon migration played an important role in the evolution of the carbonate caprock.
10	Nokhbatolfighahaei et al. (2019)	Dolostone in Dehkoye and Paskhand salt diapirs, Hormuz Complex, Southern Iran	Field observations, petrographic analysis, geochemical analysis, mineralogic analysis; C and O isotopic studies, fluid inclusion	Four dolomite types were identified: very fine-to-fine crystalline dolomite (D1), neomorphic dolomite (D2), fine-to-medium crystalline euhedral-to-subhedral dolomite (D3), and pore- and fracture-filling dolomite (D4). The oxygen and carbon isotope values suggest different formation conditions- D1 dolomites formed under low temperatures (~70 °C) and D3 and D4 dolomites forming under higher temperatures (~270 °C). The primary sources for secondary dolomites are deeper hydrothermal and catchment sources, ascending through faults during intrusion. Meteoric waters are considered less significant sources. The presence of the mineral sassolite (B(OH)3) in the Deh-kuyeh salt diapir suggests fumarolic activity and extensional tectonics.
11	Caesar et al. (2019)	dolostone in the deposition of carbonate in northern Gulf of Mexico Basin salt structures, USA	Field observations, petrographic analysis; S, C and O isotopic analysis; mineralogical analysis; clumped isotope	Carbonate formation in salt diapir cap rocks is significantly influenced by microbial anaerobic oxidation of methane (AOM). Sulfur isotope data indicate that cap rock mineral precipitation occurred via closed-system sulfate reduction. The $^{13}\text{C}$ -depleted carbonate carbon isotope

(continued on next page)

Table 1 (continued)

No.	Author(s)	Terrain & Country	Approaches	Keys conclusion
12	Kernen et al. (2020)	Origin of the Neoproterozoic rim dolomite as lateral carbonate caprock, Patawarta salt sheet, Flinders Ranges, South Australia	Detailed field mapping, stratigraphic analysis, petrographic analysis	compositions (−52.7 to −2.9‰) and low clumped isotope-derived carbonate formation temperatures (26–83 °C) support the role of microbial AOM in carbonate formation. The rim dolomite at the Patawarta diapir is interpreted as a lateral carbonate caprock that formed at the salt-sediment interface. This caprock developed through the dissolution of halite and accretion of insoluble residues. Four capstone fabrics were identified in the rim dolomite: massive, porphyritic, banded, and brecciated, which resembles Poe et al.'s (2018) classification. The caprock initially formed in a crestal position and was later rotated to a lateral position due to diapiric inflation and folding of the overlying strata. Episodes of hydrocarbon migration played an important role in the evolution of the carbonate caprock.
13	Aftabie et al. (2022)	Glaciogenic origin of the carbonate deposits of Hormuz Island, southern Iran	Field observations, petrographic analysis Isotopic analysis (C and O) Geochemical analyses	Various types of clasts within the diamictites and dropstones in the cap carbonates supports Ediacaran glaciation during deposition of Hormuz carbonates. The depositional environment involved significant hydrothermal contributions, leading to increased seawater alkalinity and carbonate precipitation under reducing conditions. This was influenced by submarine glaciovolcanism and exhalative high temperature hydrothermal systems (~252.7 °C), associated with the Snowball Earth conditions of the Ediacaran time.
14	Adineh et al. (this study)	Dolostones in Paskhand salt diapir, Hormuz Complex, south Iran	Field observations, Petrographic, mineralogic, isotopic (C and O) and clumped isotopic analysis	Dolomitic micritic dolomite, three types of matrix dolomites and two types of cement dolomites, with minor other cement phases were identified. Most dolomite types formed at both low (<~100 °C) and high temperatures (~100–300 °C), indicating different dolomitization stages. The $\delta^{13}\text{C}$ and $\delta^{18}\text{O}$ ranges of the dolomites overlapped with the then seawater, suggesting that the dolomitizing fluids were recycled seawater. Hydrothermal fluids played a crucial role, as indicated by the presence of minerals e.g., muscovite, rhodochrosite, phlogopite, rutile, chlorite, apatite and tourmaline. Hydrothermal fluids were $\text{Mg}^{2+}$ -depleted, and the presence of quartz and calcite suggested mixing with siliceous fluids from igneous rocks/siliciclastic deposits. The study highlighted the complex interplay between volcanism, hydrothermal activity and seawater in dolomite recrystallization during the Late Ediacaran.

outcrop of the late Ediacaran cap carbonates within the Paskhand salt diapir (Fig. 4F). The cap carbonate was deposited in a lagoon within an extensional back-arc basin during the late Ediacaran period (Adineh et al., 2023).

### 3. Methods

The 1/10,000 BASTAK map sheet (Farzipour Saeen et al., 2007) served as the base map for this study. The background shaded relief in the geological maps was generated using the ASTER Global Digital Elevation Model (GDEM) (<https://earthdata.nasa.gov/learn/articles/new-aster-gdem>). Lithologic and structural mappings were conducted on the Paskhand diapir by Adineh et al. (2023, 2024). Rock samples were collected from various parts of the carbonate megaclasts from stratigraphic successions at the surface of an emergent Paskhand salt

diapir, including host rock and veins. The sample location is shown in Fig. 3A. Hundred representative rock samples were thin-sectioned and 41 were analyzed geochemically.

#### 3.1. Petrography

Salt diapirs can be associated spatially with dolomitization (Table 1). A petrographic examination using both transmitted and reflected lights revealed a two-phase dolomitization: (i) fabric-preserving dolomites (Fig. 5), and (ii) non-fabric preserved dolomite (Figs. 6–8) and later dolomitic cementation (Fig. 9). Different types of dolomites in the Hormuz Complex were identified based on the shape of crystal boundaries and the size distribution of crystals, following the classification system (Sibley and Gregg, 1987). Additionally, the analysis with transmitted and reflected light microscopy allowed the identification of other

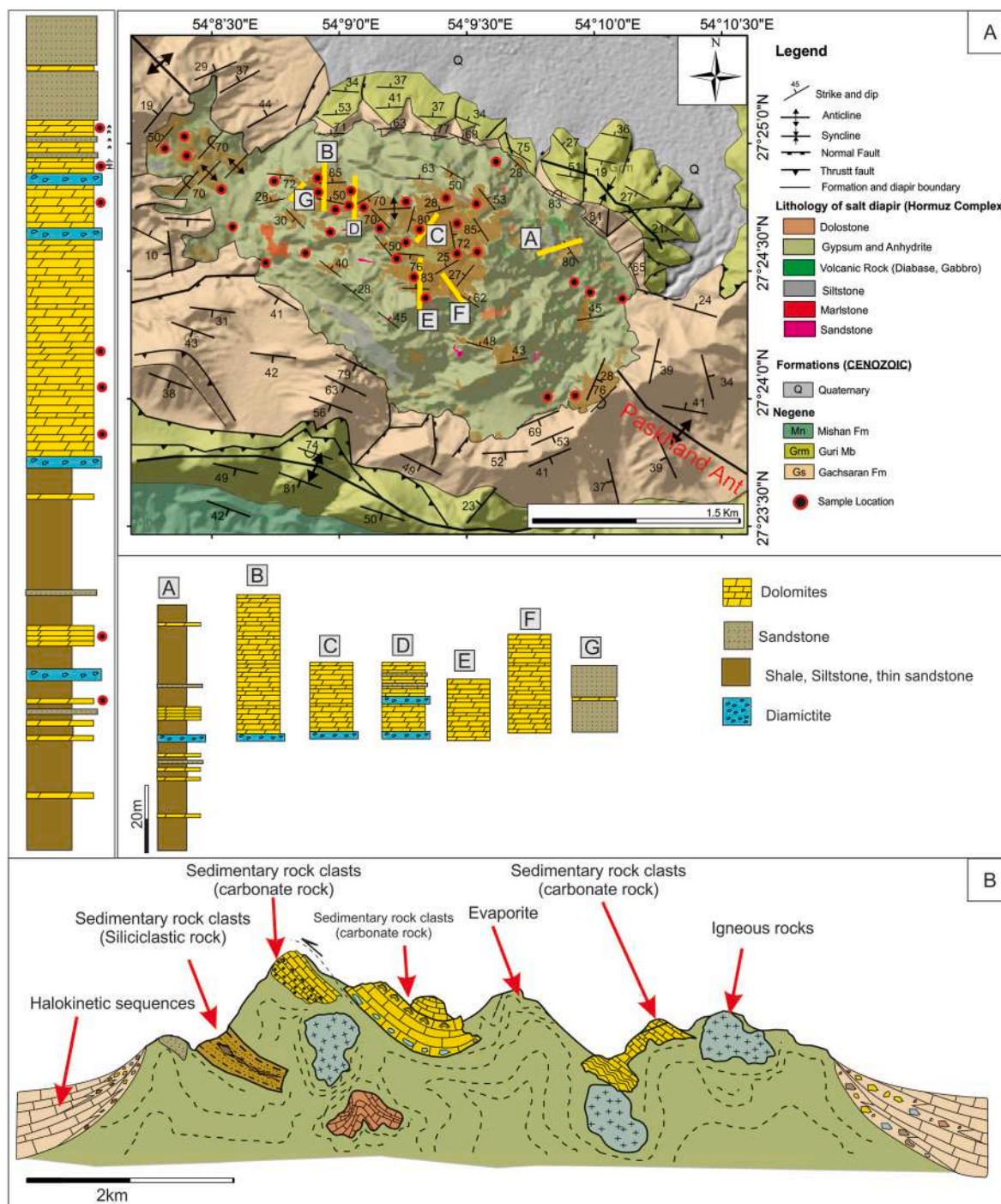


Fig. 3. A. Lithological map of the caprock of the Paskhand salt diapir and sedimentary successions around the diapir (modified after Adineh et al., 2024; Závada et al., 2021). B. Idealized stratigraphic column of the Hormuz carbonates, reconstructed from carbonate exotic blocks observed at the top of the diapir. C. Schematic cross-section of the Paskhand salt diapir, featuring exotic blocks embedded within a gypsum matrix.

significant minerals associated with high-temperature dolomitization (HTD) and geologic events such as karstification, the formation of Mississippi Valley-type minerals, breccias and vugs resulting from solution activity.

### 3.2. SEM analysis

We also used Back Scattered Electron (BSE) imaging and identified phases using a scanning electron microscope (SEM Tescan VEGA) at the Institute of Petrology and Structural Geology (Faculty of Science, Charles University, Prague). The SEM is equipped with an energy

dispersive spectroscope (EDS X-Max 50, Oxford Instruments) operating with 15 kV accelerating voltage and 1.5 nA beam current.

### 3.3. C, O & clumped isotope analysis

Supplementary Table 1 presents the results of the C, O and clumped isotope analysis. Samples were analyzed at the Laboratoire des Sciences du Climat et de l'Environnement (LSCE) (standard procedure as per Daéron, 2021). Carbonate samples were converted to CO<sub>2</sub> by phosphoric acid reaction at 90 °C in a common, stirred acid bath for 30 min. Initial phosphoric acid concentration was 103% (1.91 g cm<sup>-3</sup>) and each batch

**Table 2**

Isotopic geochemical results on different types of dolomites. This table presents the  $\delta^{13}\text{C}$ ,  $\delta^{18}\text{O}$ , and  $\Delta_{47}$  values along with their ranges and averages for various dolomite sample types (LMD, D1, D2, D3, CD1, SD and CAL). It also provides the corresponding temperature ranges. The number of samples for each type is denoted by 'N'.

Sample	N	$\delta^{13}\text{C}_{\text{VPDB}}$ range	$\delta^{13}\text{C}_{\text{VPDB}}$ average	$\delta^{18}\text{O}_{\text{VPDB}}$ range	$\delta^{18}\text{O}_{\text{VPDB}}$ average	$\Delta_{47}$ range	$\Delta_{47}$ average	Temperature range ( $^{\circ}\text{C}$ )	Temperature average ( $^{\circ}\text{C}$ )
LMD	5	-6.74 to -2.92	-4.18	-14.29 to -4.09	-6.63	0.301 to 0.490	0.354	67.9 to 218.9	169.8
D1	7	-5.63 to 2.38	-0.25	-14.29 to -3.15	-6.57	0.301 to 0.357	0.332	154.7 to 218.8	180.8
D2	8	-3.40 to 1.93	0.10	-6.45 to -2.78	-4.42	0.299 to 0.390	0.341	127.1 to 220.7	172.9
D3	6	-1.05 to 1.51	-0.03	-8.95 to 2.98	-3.11	0.325 to 0.426	0.376	102.2 to 187.5	140.5
CD1	5	-3.88 to 1.73	-0.09	-4.39 to -1.80	-3.18	0.329 to 0.435	0.373	96.5 to 183.6	145.9
SD	6	-6.32 to 0.55	-3.25	-7.91 to -2.86	-5.18	0.320 to 0.450	0.367	87.9 to 193.8	150.3
CAL	4	-7.19 to -0.28	-3.01	-4.33 to -2.23	-3.19	0.539 to 0.588	0.557	29.3 to 46.5	40.2

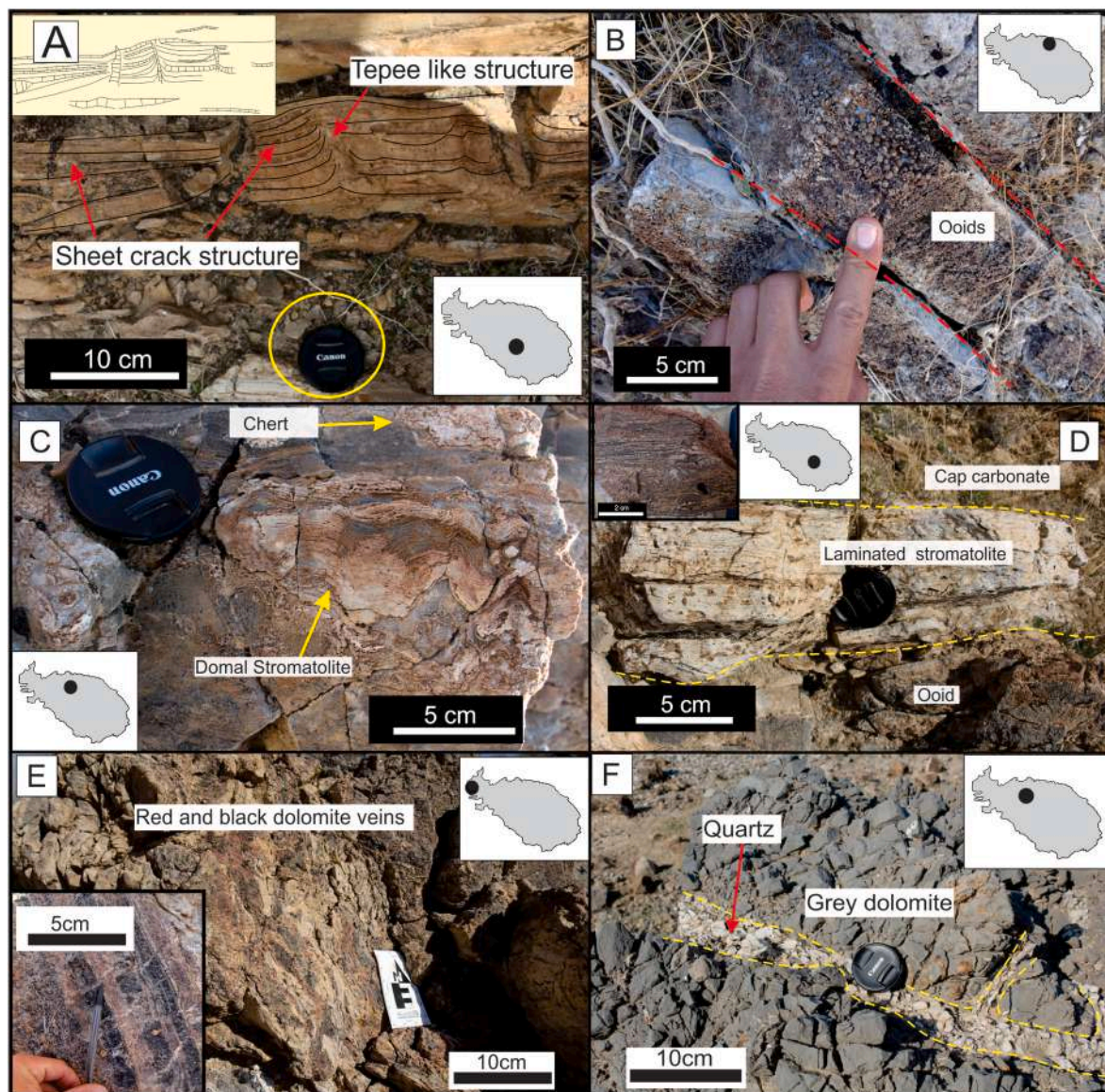


**Fig. 4.** Characteristics of late Ediacaran cap carbonate of Hormuz Complex. A. Teepee like and sheet crack structures. B. Ooiditic dolostone. C. Domal stromatolitic dolostone. D. Laminated stromatolitic dolostone. E. Red and black dolomite veins in the late Ediacaran cap carbonate. F. Quartz veins observed in the late Ediacaran cap carbonate.

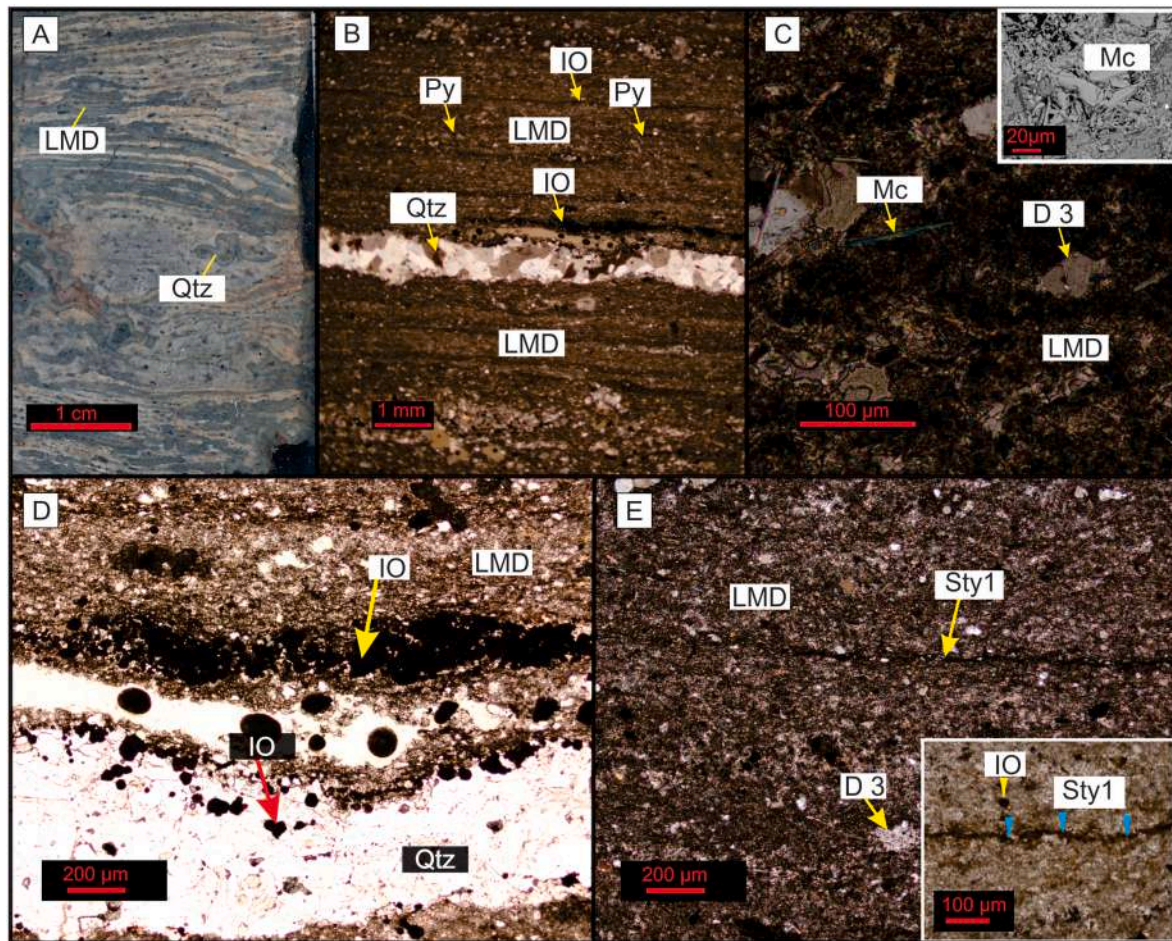


**Fig. 5.** LMD crystalline. **A.** Hand sample photograph of horizontal laminate. **B.** photomicrography of very finely laminated crystalline dolomite (MLD), with finely anhedral to subhedral crystals; cross polarized light. **C.** photomicrograph for LMD dolomite with Mica and D3, cross polarized light. **D.** photomicrograph for LMD with Iron oxide and quartz veins which is parallel to the lamination of LMD, cross polarized light. **E.** Stylolite parallel to the LMD crystalline, plane polarized light.

of acid was used for seven days. After cryogenic removal of water, the evolved  $\text{CO}_2$  was helium-flushed at  $25 \text{ mL min}^{-1}$  through a purification column packed with Porapak Q (50/80 mesh, 1 m long, 2.1 mm inner diameter (ID) and at  $\sim 20^\circ \text{C}$ , then quantitatively recollecting by cryogenic trapping and transferred into an Isoprime 100 dual-inlet mass spectrometer equipped with 6 F collectors ( $m/z$  44–49). Each analysis took  $\sim 2.5$  h, during which analytic gas and working reference gas were allowed to flow from matching, 10 mL reservoirs into the source through deactivated fused silica capillaries (65 cm long,  $110 \mu\text{m}$  ID). After every 20 min, and for a total time of  $\sim 150$  min, gas pressures were adjusted to achieve  $m/z = 44$  current of 80 nA, with differences between analytic gas and working gas generally  $< 0.1$  nA. Pressure-dependent background current corrections were measured 12 times for each analysis. All background measurements from a given session within  $\pm 6$  h of any given analysis were used to determine a mass-specific relationship for that analysis, linking background intensity ( $Z_m$ ), total  $m/z = 44$  intensity ( $I_{44}$ ), and time ( $t$ ):  $Z_m = aI_{44} + P(t)$ . 'P' is a polynomial of degree 2 to 4. Background-corrected ion current ratios ( $\delta_{45}$  to  $\delta_{49}$ ) were converted to  $\delta^{13}\text{C}$ ,  $\delta^{18}\text{O}$  and "raw"  $\Delta_{47}$  values as described by Daëron et al. (2016) using the IUPAC oxygen-17 correction parameters (Brand et al., 2010). The isotopic compositions ( $\delta^{13}\text{C}$ ,  $\delta^{18}\text{O}$ ) of our working reference gas was computed based on the nominal isotopic composition of all ETH carbonate standards (Bernasconi et al., 2018) and an oxygen-18 acid fractionation factor of 1.00813 (Kim et al., 2007). Raw  $\Delta_{47}$  values were then converted to the I-CDES reference frame (Bernasconi et al., 2021) by pooled regression (Daëron, 2021) as implemented by the D47 crunch Python library (3.9 VERSION and

2021). Full analytical errors are derived from the external reproducibility of unknowns and standards ( $N_f = 76$ ) and conservatively account for the uncertainties in raw  $\Delta_{47}$  measurements as well as those associated with the conversion to the I-CDES reference frame (Daëron, 2021).

## 4. Results

### 4.1. Petrography & distribution of diagenetic phases

According to the sizes, distributions and boundary shapes (planar and nonplanar) of the crystals, as detailed by Gregg and Sibley (1984, 1987), six major types of dolomites (D) have been identified. These are further classified into three primary categories: laminated micritic dolomites, matrix dolomites and dolomite cements.

#### 4.1.1. Laminated micritic dolomite/microbial-laminated dolomites (LMDs)

In hand specimens, MLD is a grey to light grey and maintain well-preserved primary fabrics including laminations and with precursor carbonate grain structures (Fig. 5A–E). This dolomite is sampled from stromatolitic dolomites (Fig. 4C and D). This dolomite is dense and nonporous, composed of (very) fine anhedral to subhedral crystals with  $5\text{--}24 \mu\text{m}$  sizes, with  $\sim 12 \mu\text{m}$  as the average. The crystals typically display nonplanar-a to planar-s textures (Fig. 5A–E). Occasionally, slightly coarser dolomite crystals (D3;  $100\text{--}200 \mu\text{m}$ ), which frequently exhibit more planar-s crystal surfaces, are distributed irregularly within the MLD matrix, resulting in a bimodal crystal pattern.

The laminated quartz and iron oxide crystals are interbedded with

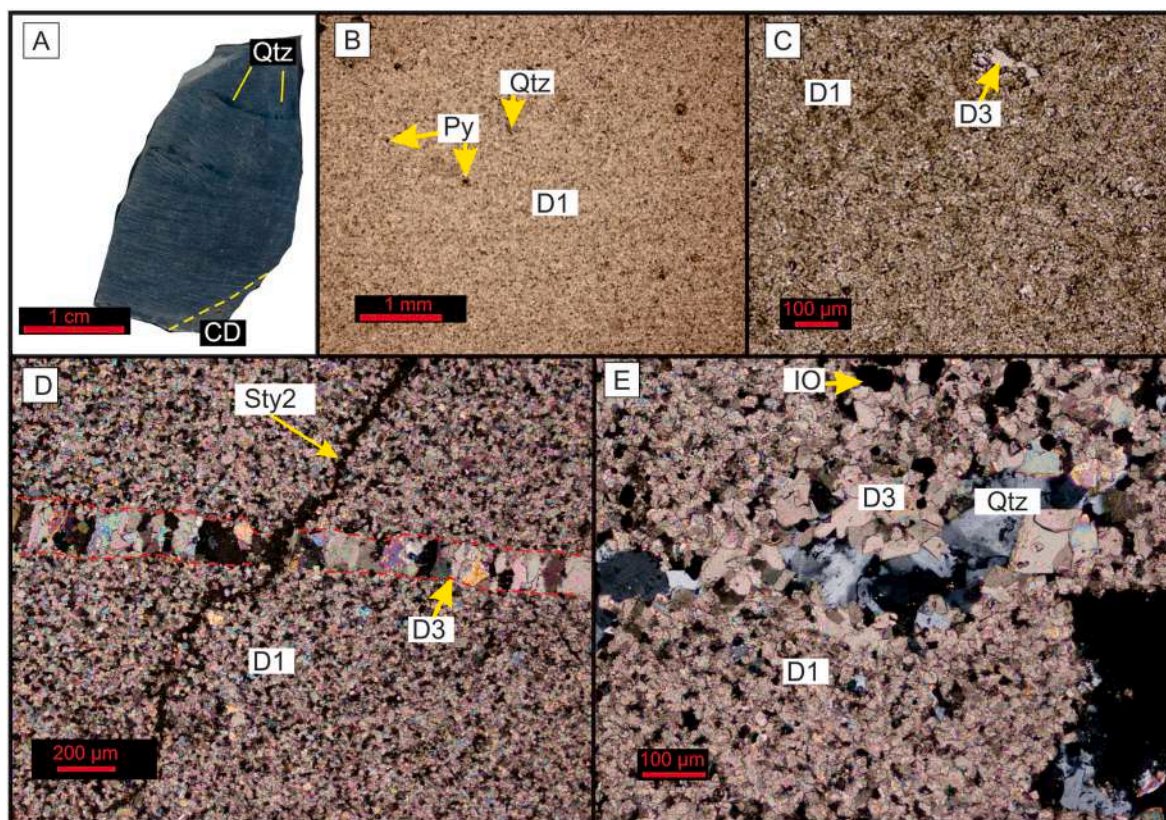


**Fig. 6.** D1 dolomite. **A.** Hand sample photograph of D1 with quartz veins and porosity which is filled by CD. **B.** D1 with intercrystalline porosity which is filled by pyrite and quartz; cross polarized light. **C.** with intercrystalline porosity which is filled by D3. **D.** Stylolite cross cutting the D1 and the fracture which is filled by D3, plane polarized light. **E.** fractures cross cutting D1 and iron oxide; plane polarized light.

dolomitic crystals (Fig. 5B–D). Cryptocrystalline to crystalline pyrites, iron oxides, quartz and micas are commonly dispersed within intercrystalline pores (Fig. 5C). In some areas, stylolites (Sty1) with low amplitude cut across the dolomite crystals (Fig. 5E). This type of dolomite is typically found within laminated dolomites in the Paskhand salt diapir. This dolomite variety accounts for ~10% of the dolomite rocks based on outcrop and thin-section studies.

#### 4.1.2. Matrix dolomites

**4.1.2.1. Very finely to finely crystalline, nonplanar-a to planar-s dolomites (D1).** Dark grey D1 dolomites are heavier (Fig. 6A). Under an optical microscope, D1's crystals range 30–100 μm in size, with an average size ~60 μm, and commonly exhibit planar-s to nonplanar-a textures (Fig. 6B–E). Unlike the LMD, D1 dolomitization destroys the original fabrics. D1 dolomite is characterized by textures ranging from planar-s to planar-e, with limited intercrystalline porosity or fractures, which are often filled with slightly coarser dolomites (D3), resulting in bimodal crystal sizes (Fig. 6D and E). However, most thin sections typically show unimodal crystal patterns. In some regions, dolomite crystals are intersected by stylolites (Sty2; Fig. 6D). Additionally, pyrites, iron oxides and cryptocrystalline to crystalline quartz forms are frequently found dispersed within the intercrystalline porosity (Fig. 6). This type of dolomite constitutes ~40% by volume based on outcrop and thin-section studies. It generally occurs as thick laminated dolomite formations.

**4.1.2.2. Finely to medium crystalline planar-a(s) dolomite (D2).** In hand specimens, D2 dolomites are characterized by alternating light to dark grey laminae and are porous (Fig. 7A). This dolomite is sampled from oolitic dolomite (Fig. 4B) Thin section analysis reveals that the majority

of dolomite crystals are between 60 and 200 μm in size, with some reaching up to 300 μm and often containing ghost grains (Fig. 7A–E). Under polarized light (PPL) and cross-polarized light (XPL), these crystals typically show planar-a(s) textures and pronounced extinction, with surfaces frequently containing impurities (Fig. 7D and E). Occasionally, crystals with clear surfaces or bright edges display nonplanar-a textures and slightly undulatory extinction (Fig. 7D and E). The tightly packed crystals form a mosaic texture, with minimal iron oxide remaining in the intercrystalline pores.

D2 dolomites can be further classified into three primary lithologic assemblages within the Late Ediacaran-Cambrian carbonates. The first assemblage consists of 0.5–1 m thick thin beds often interbedded with D1 dolomites. The second assemblage appears as bimodal dolomites, frequently coexisting with D1, and can be 4–10 m thick. The less commonly developed third assemblage (<5 m thick) is typically found overlying the MLD. D2 comprises ~10% of the total dolomite area.

**4.1.2.3. Medium to coarsely crystalline nonplanar-a dolomites (D3).** In hand specimens, D3 dolomites are light grey or grayish-white, suggesting significant thermal fading. The dolomite crystals exhibit irregular or indented boundaries with the preceding D1 dolomites (Fig. 8). Pores occur in these specimens, and some are arranged linearly (Fig. 8A). The crystals range from medium to coarse size, between 200 μm and 1 mm. Most crystals display nonplanar-a textures, with a few exhibiting planar-s textures and slight undulating extinction (Fig. 8A–E). The D3 dolomites appear hazy under an optical microscope due to abundant inclusions (Fig. 8C). This dolomite type is predominantly fabric-destructive, obscuring original depositional and early diagenetic features. D3 dolomite crystals are characterized by a central dirty surface, with some areas showing clean edges within the crystal (Fig. 8B and C). In certain samples, D3 dolomites are intersected by stylolite or fractures (Sty3 in

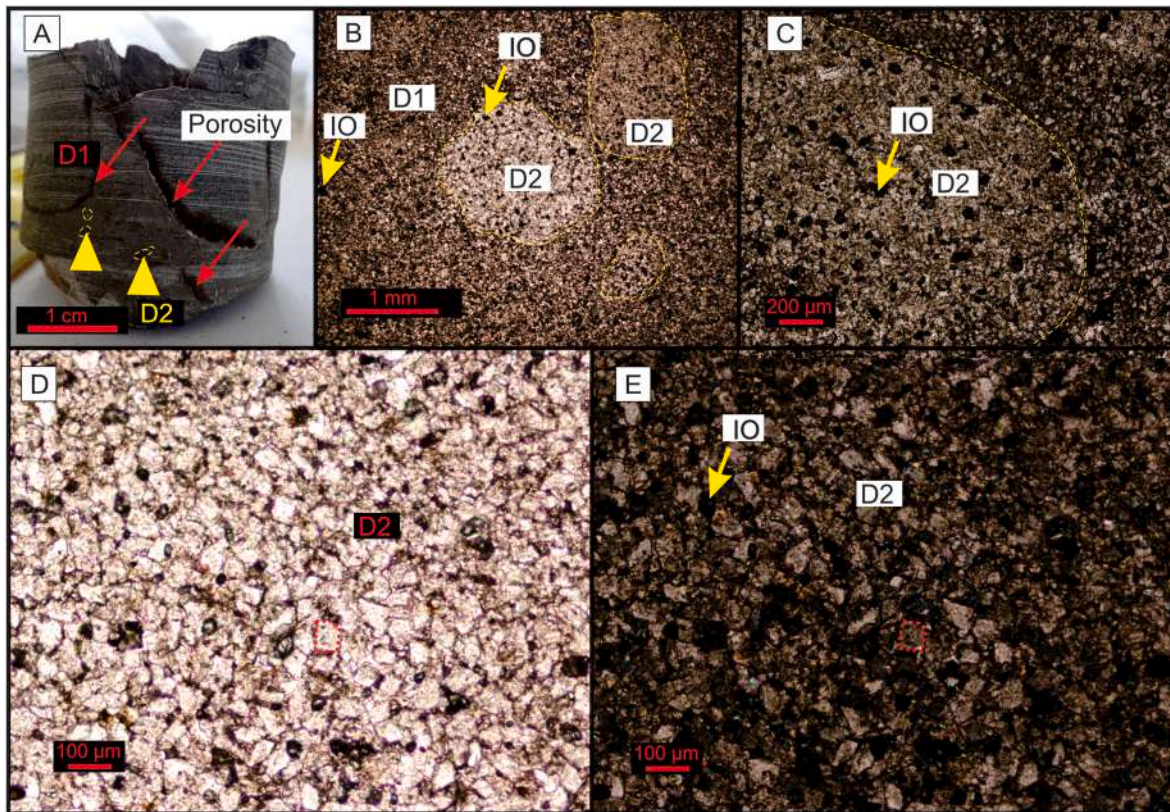


**Fig. 7.** D2 dolomite. **A.** hand sample photograph showing D2 as being dark circular dolomitized ooids in the laminated D1 as being laminated micritic dolomite with a few fractures. **B & C.** Photomicroscopy of finely to medium crystalline dolomite (D2), with planar-s textures, iron oxide (IO) disseminated extensively in the intercrystalline pores within the very finely to finely dolomite crystals (D1), which is displaying bimodal crystal clusters. Cross-polarized light (XPL). **D & E.** Paired photomicrographs of D2 dolomite displaying unimodal crystal clusters with scattered iron oxide crystals (arrows) within intercrystalline in the ooid. **(D)** PPL **(E)** XPL.

**Fig. 8B and C).** This dolomite is associated mainly with the fracture systems of the upper strata, particularly at the edge of the diapir. based on outcrop and thin-section studies, D3 dolomite accounts for <10% of the total dolomite area.

#### 4.1.3. Cement dolomites (CD)

In hand specimens, this variety of dolomites are milky-white to light red, reflecting noticeable thermal fading (Fig. 9A). The cement dolomite includes both CD1 and saddle dolomite (SD or CD2) varieties. CD1 predominantly develops along fracture systems or within broken breccia spaces of the Late Ediacaran-Cambrian Hormuz dolostone samples (Fig. 9B–D). The SD variety occurs inside pores created by dissolution (Fig. 9E).

CD1 typically occur as the initial cement and/or lining within fractures and is arranged linearly (Fig. 9). Crystals in D3, commonly 200 μm to 1 mm in size, is characterized by a medium to coarse crystalline structures with nonplanar-s/e textures and undulatory extinction under both plane and cross-polars (Fig. 9B–D). CD1 shows embayed contacts with the host rock or breccias and tends to partially or completely fill the pores (vugs) (Fig. 4E). In thin sections, CD1, similar to D3, is characterized by curved boundaries and undulatory extinction (Fig. 9B). Whereas the SD is present pervasively, CD1 is less abundant, sometimes acting as a nucleus for the SD crystals (Fig. 9E). SD exhibits alternating color bands with saddle or baroque-shaped crystals (Fig. 9A). Under plane-polarized light, SD crystals display central dirty nuclei with bright edges (Fig. 9B). Overall, CD constitutes of <20% of the total dolomite area.

#### 4.1.4. Late-stage calcite & silica cements

Silica cement is commonly found to fill up fractures or vugs, often along with matrix dolomites or CD1 (Fig. 10). In some cases, chalcidony

fills the fractures after the CD1 (Fig. 10). The structure of quartz crystals varies from microcrystalline to granular (Fig. 10). Calcite primarily appears in the residual pores or fractures that remain after the filling by D3 or CD (Fig. 9D and 10D). In a few cases, quartz and iron oxides are associated spatially (Fig. 4E and 9A).

#### 4.2. Mineralogical observations

The backscattered electron (BSE) images (Fig. 11) reveal the mineralogical assemblages observed in the different types of samples. The analysis revealed that different types of dolomites exhibit a wide range of mineral compositions. However, no clear relationship could be established between dolomitization and mineralization. Additionally, it was observed that various types of dolomites display similar mineralogical characteristics, indicating a lack of distinct mineral signatures associated with specific dolomitization processes. However, certain minerals e.g., pyrites and iron oxides, were mainly observed to be smaller in size (<24 μm) in fabric-preserving dolomites (Kent, 1979; Nasir et al., 2008; Aftabi et al., 2022) (Fig. 4C and D). In contrast, these minerals predominantly fill pores in other types of dolomites (Fig. 11D). The matrix is predominantly composed of dolomites (D1) and quartz (Qz), with notable inclusions of hematite (Hem) and rhodochrosite (Rds) (Fig. 10A). D2–D3 are associated with rutile (Rt) and chlorite (Chl), along with tourmaline needles (Tur) (Fig. 10B). Fig. 10C highlights the coexistence of D2 with calcite (Cal) and apatite (Ap), illustrating multiple occurrences of apatite within the calcite matrix. Pyrite (Py) inclusions occur within the quartz and dolomite framework (D3 and CD1) (Fig. 10D). Fig. 10E displays talc (Tlc) and phlogopite (Phl) interspersed among the dolomite grains (D2), indicating complex mineral interactions. Fig. 10F reveals well-formed SD crystals with significant intergrowths and zoning, where the lighter parts indicate higher

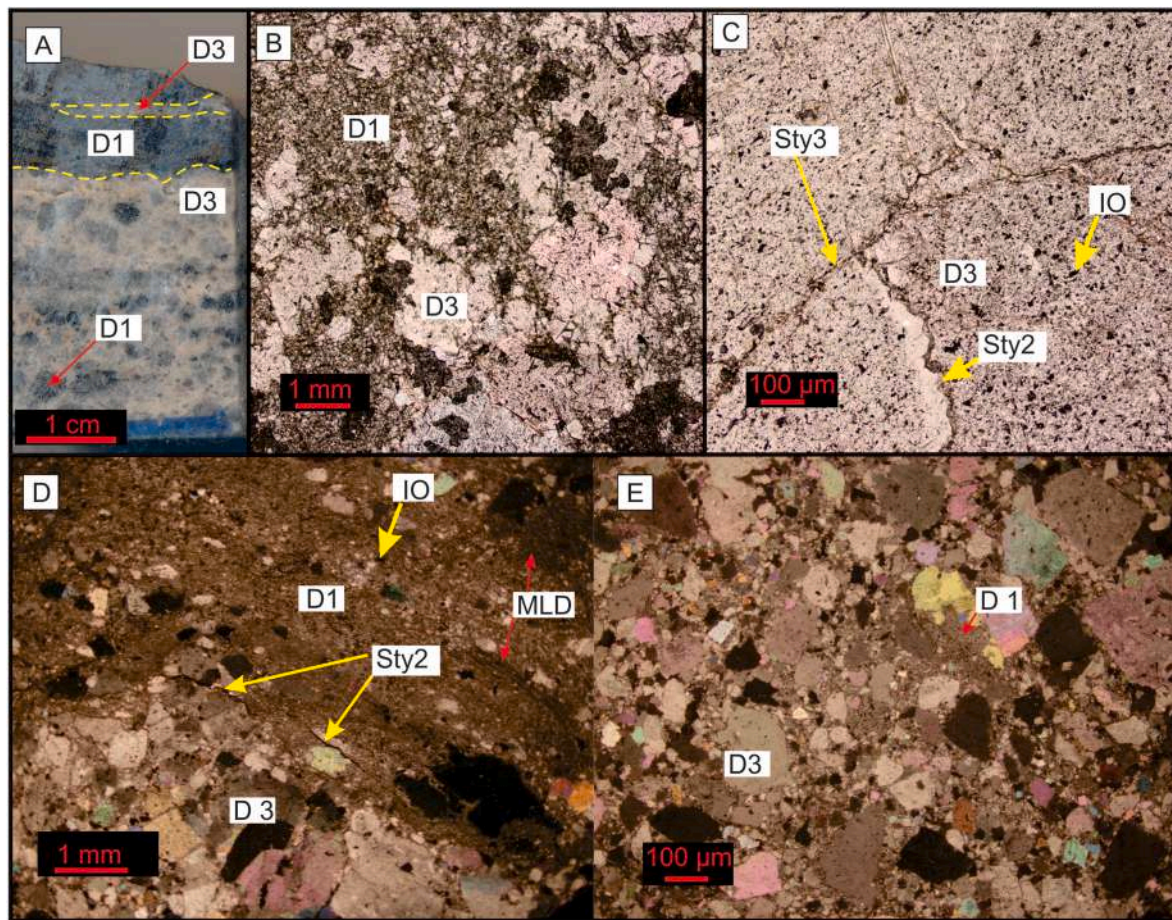


**Fig. 8.** D3 dolomite. A) hand sample photograph showing D3 as white or light grey dolomite, which is filling the fractures crosscutting the D1. B. D1 dedolomitized by D3. C. stylolite crosscutting the D3 dolomite (PPL). D-E. D3 dolomite is associated with IO, LMD, D1 (XPL).

magnesium concentration.

#### 4.3. Isotopic geochemistry

Supplementary Table 1 presents the geochemical data set of this study. Table 2 summarizes the  $\delta^{13}\text{C}$ ,  $\delta^{18}\text{O}$ , and  $\Delta_{47}$  values and temperature ranges and averages, for various dolomite sample types (LMD, D1, D2, D3, CD1, SD and CAL).

In our study, the C and O isotope data were analyzed to understand the isotopic variations across different types of dolomite (Fig. 12A). The first graph (Fig. 12A) compares  $\delta^{13}\text{C}_{\text{VPDB}}$  and  $\delta^{18}\text{O}_{\text{VPDB}}$  values, revealing overlap between groupings of dolomite types (Fig. 12A). The second graph (Fig. 12B) presented  $T^{\circ}\text{C}$  values plotted against  $\delta^{18}\text{O}_{\text{VPDB}}$  (Fig. 12B). The third graph (Fig. 12C) focused on the relationship between  $T^{\circ}\text{C}$  and  $\delta^{13}\text{C}_{\text{VPDB}}$ . Fig. 12D depicts  $\delta^{18}\text{O}_{\text{fluid}}$  (VSMOW, ‰) as a function of temperature ( $^{\circ}\text{C} \pm 95\%$ ), with fields denoted for comparison with modern formation fluids and Ediacaran clumped isotope data from Loyd et al. (2015).

## 5. Discussions

### 5.1. Origin of LMD

The LMD, distinguished by its very fine dolomite crystal size ( $<24\ \mu\text{m}$ ), generally forms in low-energy, restricted sedimentary settings (e.g., Zhang et al., 2024), which suggests it represents the initial phase of dolomitization. In addition, the presence of low-amplitude stylolites within the LMD (Fig. 5E) indicates that the LMD is less compacted but did not reach the critical burial depths typically associated with

extensive stylolites (Qing and Mountjoy, 1989, 1994; Tucker and Wright, 2009; Machel, 1999; Jacquemyn et al., 2014). The limited formation of stylolites within the LMD indicates a shallow burial environment with restricted depth under low-temperature conditions (e.g., Moore, 2013). Therefore, the LMD began to form almost immediately after the sediment was deposited and continued to develop during the early stages of burial, but before significant compaction or deeper burial occurred. In addition, the well-preserved fabrics (microbial or grainy) and the very fine to fine anhedral to subhedral crystals, ranging in size from 5 to 24  $\mu\text{m}$  in the LMD, suggest that these fabrics developed slowly under low temperatures (Gregg and Sibley, 1984, 1987; Warren, 2000; Yang et al., 2017), indicating that dolomitization began at an early stage (Zhou et al., 2017). However, clumped isotope analysis shows that most of the LMD dolomite recrystallized at high temperatures (average 169.8  $^{\circ}\text{C}$ ) while preserving its original fabrics. This suggests that these dolomites underwent significant thermal alteration likely associated with hydrothermal activity at a very stage of replacive dolomitization of precursor sediments.

The negative carbon isotopic values ( $\delta^{13}\text{C}_{\text{VPDB}}$ : 6.74 to  $-2.92\text{‰}$ ) indicate that the dolomitizing fluids were likely influenced by organic-rich environments, which possibly correlate with the Ediacaran biota at the onset of the Shuram excursion (Aftabi et al., 2022).

The oxygen isotopic composition of the LMD ( $\delta^{18}\text{O}_{\text{VPDB}}$ : 14.29 to  $-4.09\text{‰}$ ) suggests that the hot dolomitizing fluids responsible for its formation possibly originated within a shallow burial environment, as supported by the presence of low-amplitude stylolites.

During the late Ediacaran to Early Cambrian, the Hormuz Basin was situated at a paleo latitude of 20–30° S (Allen, 2007), which is characterized by a (semi)arid climate (Nasir et al., 2008). The Hormuz basin is

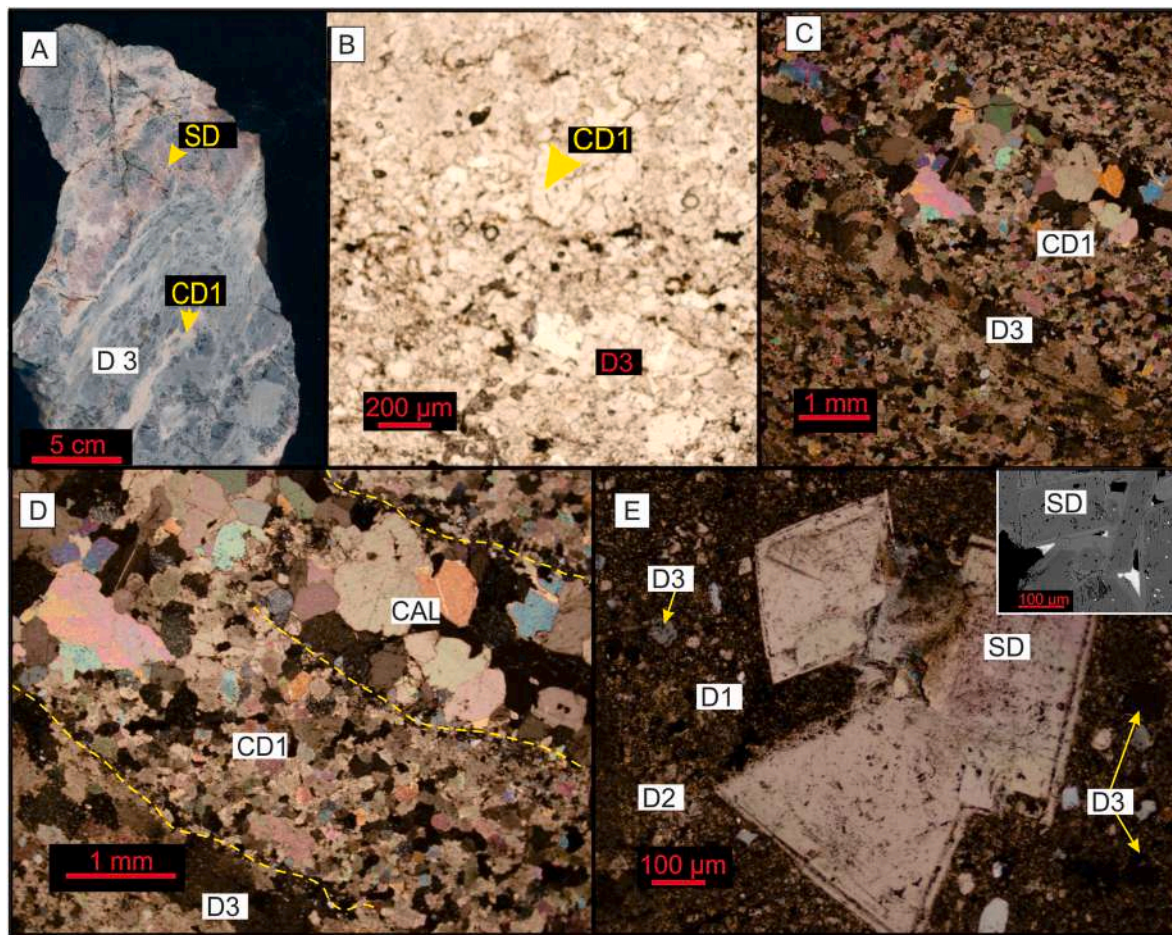


Fig. 9. Cemented dolomite (CD1 and SD). A. hand sample photograph showing grey dolomite (D3) with red and white dolomitic veins (CD1 and SD). B. CD1 and D3 (PPL). C. CD1 and D3 (XPL). D. Fracture crosscutting D3 which is filled by CD1 and CAL (XPL). E. SD surrounded by D1-D3 (XPL).

separated from open sea by an arc belt (Asadi Sarshar et al., 2022). Due to the restricted exchange between the platform interior and the open sea, the salinity level of seawater increased under these conditions due to evaporation. The supply of  $Mg^{2+}$ , driven by volcanic activities, led to the deposition of dolomite in the Hormuz basin. The continuous process of dolomitizing fluids moving into and through the rock with increasing temperatures can enhance dolomite precipitation and the formation of early nuclei (Schmoker and Halley, 1982; Machel, 2000). Small pyrite crystals within the intercrystalline pores of LMD (stromatolitic dolomite) suggest bacterial sulfate reduction (BSR) or thermochemical sulfate reduction (TSR) might have played a role in dolomite nucleation in the Hormuz basin (Fig. 5) (Ghazban and Al-Aasm, 2010). The presence of minerals e.g., muscovite, rhodochrosite, phlogopite, rutile, chlorite, apatite and tourmaline indicate that the hydrothermal activity originated from contemporaneous volcanic events during the Late Ediacaran to Cambrian Period (Fig. 11). The evaporite layers overlying the dolomite may have acted as a barrier to fluid movement, creating a relatively closed system that limited external fluid interactions. As a result, the original isotopic geochemical characteristics of the dolomite were likely preserved, minimizing significant alteration during diagenesis.

## 5.2. Origin of D1 dolomites

The presence of discrete stylolites within the D1 dolomite (Fig. 6D) indicates that it was compacted less than that of the LMD, reflecting a shallow burial. The small crystal sizes (mostly  $<60 \mu m$ ) and planar-e/s textures of the D1 indicate that it experienced slow growth under low temperatures (Warren, 2000). The carbon and oxygen isotopic data

( $\delta^{13}C_{VPDB}$ : 5.63 to 2.38‰;  $\delta^{18}O_{VPDB}$ : 14.29 to  $-3.29 \text{ ‰ VPDB}$ ) show greater variability in carbon sources compared to the LMD dolomites. The wide range of  $\delta^{13}C$  values ( $-5.63$  to 2.38‰) indicates that its original fluids originated from contemporaneous seawater. The  $\delta^{18}O$  values of D1 dolomite ( $-14.29$  to  $-3.29 \text{ ‰ VPDB}$ ) largely fall within the typical marine dolomite range ( $-6.2 \text{ ‰}$  to  $-3 \text{ ‰ VPDB}$ ; Guo et al., 2021), supporting the idea that the dolomitizing fluids for D1 originated from contemporaneous seawater. Based on Table 2, the LMD and D1 dolomite yields more depleted  $\delta^{18}O$  values, indicating its formation at high temperatures. In addition, the presence of micro-sized pyrites in the intercrystalline pores suggests that bacterial sulfate reduction (BSR) or thermochemical sulfate reduction (TSR) probably played roles in nucleating dolomites in the Hormuz carbonates (Fig. 6) (Ghazban and Al-Aasm, 2010).

In contrast to the dolomite grain size, the clumped isotope analysis indicates that most of the D1 dolomite recrystallized at high temperatures (average  $180.8 \text{ }^\circ C$ ). This is likely a similar scenario to what occurred with the LMD dolomite, with the key difference being the destruction of original fabric in D1. The D1 samples appear to have undergone minimal post depositional alteration, as their average oxygen isotope values ( $-6.57 \text{ ‰}$ ) are close to or above the threshold of  $-10 \text{ ‰}$ , which is reported for the least-altered Neoproterozoic cap carbonates (Aubert et al., 2012). Based on isotopic analysis, it is believed that hot fluid circulation associated with volcanic activity degraded the organic ecosystem, increased seawater carbonate alkalinity ( $HCO_3^-$ ), and ultimately led to the hydrothermal dolomitization of the carbonate sediments. All these processes likely occurred in a closed system, which preserved the original carbon and oxygen isotopic signatures. However,

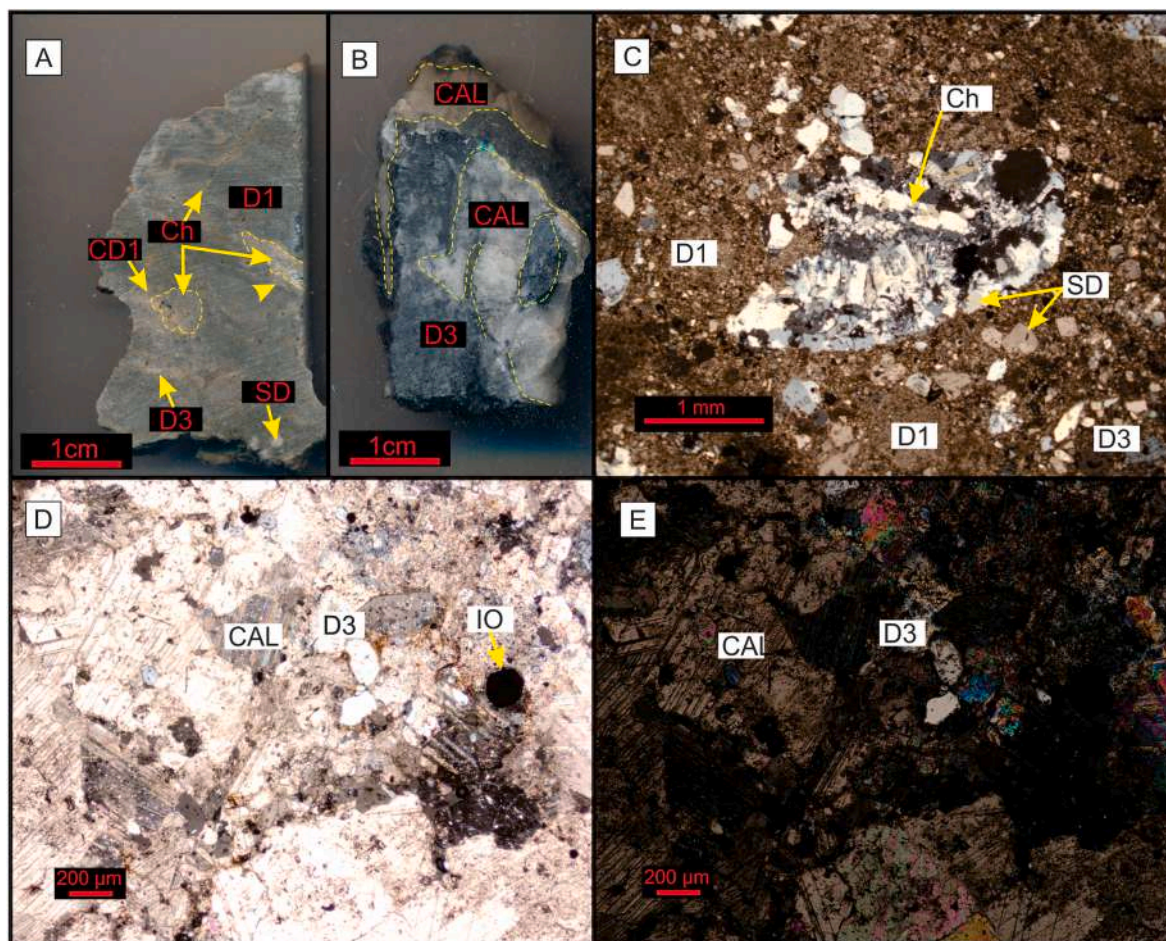


Fig. 10. Calcite and silica cement. A & B. hand sample photograph showing Calcite and silica cement veins within the dolomite. C. Silica cement (Chalcodouny) within the dolomite (XPL) D & E. Calcite veins, D- PPL, E- XPL.

clumped isotope analysis indicates high temperatures (180.8 °C) for the recrystallized dolomite, consistent with hydrothermal conditions (Montes-Hernandez et al., 2016).

### 5.3. Origin of D2 dolomites

The larger crystals and tightly packed configuration of D2 dolomite indicate that it experienced faster crystal growth than that of D1 and formed under higher temperatures (Warren, 2000, Fig. 7). The planar-a/s textures and sweeping extinctions of the dolomite crystals imply that they were formed at high temperatures (average 172.9 °C) and it does not show any stylolite evidences. These findings suggest that the replacement did not occur under typical burial conditions. Instead, it might have been triggered by the influx of Mg<sup>2+</sup>-rich exhalative hydrothermal fluids, which were released from the interaction of glacial meltwater and seawater with submarine felsic volcanism and carbonate sediments (e.g., Aftabi et al., 2022). The carbon and the oxygen isotopic data ( $\delta^{13}\text{C}$ : 3.40 to 1.93 ‰;  $\delta^{18}\text{O}$ : 6.45 to -2.78 ‰) from D2 show a wide range, indicating that the original fluids generated from a contemporaneous seawater. The more positive carbon isotope values indicate a diminished role of microbial organic activity in the recrystallization of D2, while emphasizing a greater influence of recycled coeval seawater during the late Ediacaran period. Additionally, the grain size of the dolomite is likely linked to porosity rather than temperature during hot fluid circulation, as there is a contrasting relationship between grain size and temperature compared to findings in other studies (Warren, 2000, Table 2).

### 5.4. Origin of D3 dolomites

Co-occurrence of D3 and parallel high-amplitude stylolite (Fig. 8C) suggests that D3 developed closely associated with compaction under a deep burial. Overgrowth of dolomite crystals likely developed during burial, leading to the formation of coarse-grained and even coalesced dolomite textures (Tucker and Wright, 2009). Compared to D1 and D2, D3's crystals are larger, more curved, have a nonplanar-a texture, poikilotopic contacts, undulatory extinction and are closely packed. These suggest a faster irregular crystal growth occurred at high temperatures, as confirmed by clumped isotope analysis with an average temperature of 140.5 °C. The development of larger crystals and a poikilotopic texture can be as result of the overgrowth and merging of crystals. locally similar characteristics of D3 to succedent cement dolomites (e.g., CD1) suggest same dolimitizing fluids responsible for later cement dolomites (Table 2) (Kaufman et al., 1991; Chen et al., 2004). Genesis of D3 is suggested to be closely associated with the dense conduits created by the fracture system, as evidenced by the linear arrangement of pores (vugs) observed in thin sections (Fig. 8D). The irregular or embayed boundaries between other matrix dolomites (D1 or D2) and D3 (Fig. 8) suggest involvement of dissolution or alteration. This indicates that the parental fluids of the D3 dolomite were undersaturated with respect to dolomite precipitation, meaning the fluids did not contain sufficient concentrations of magnesium and calcium ions required to promote the formation of dolomite. This undersaturation suggests that conditions were not favorable for dolomitization at that time, or that other factors, such as temperature or salinity, may have inhibited the process. The  $\delta^{13}\text{C}$  (-1.05 to 1.51 ‰) and the  $\delta^{18}\text{O}$  (-8.95 to 2.93 ‰) magnitudes of D3

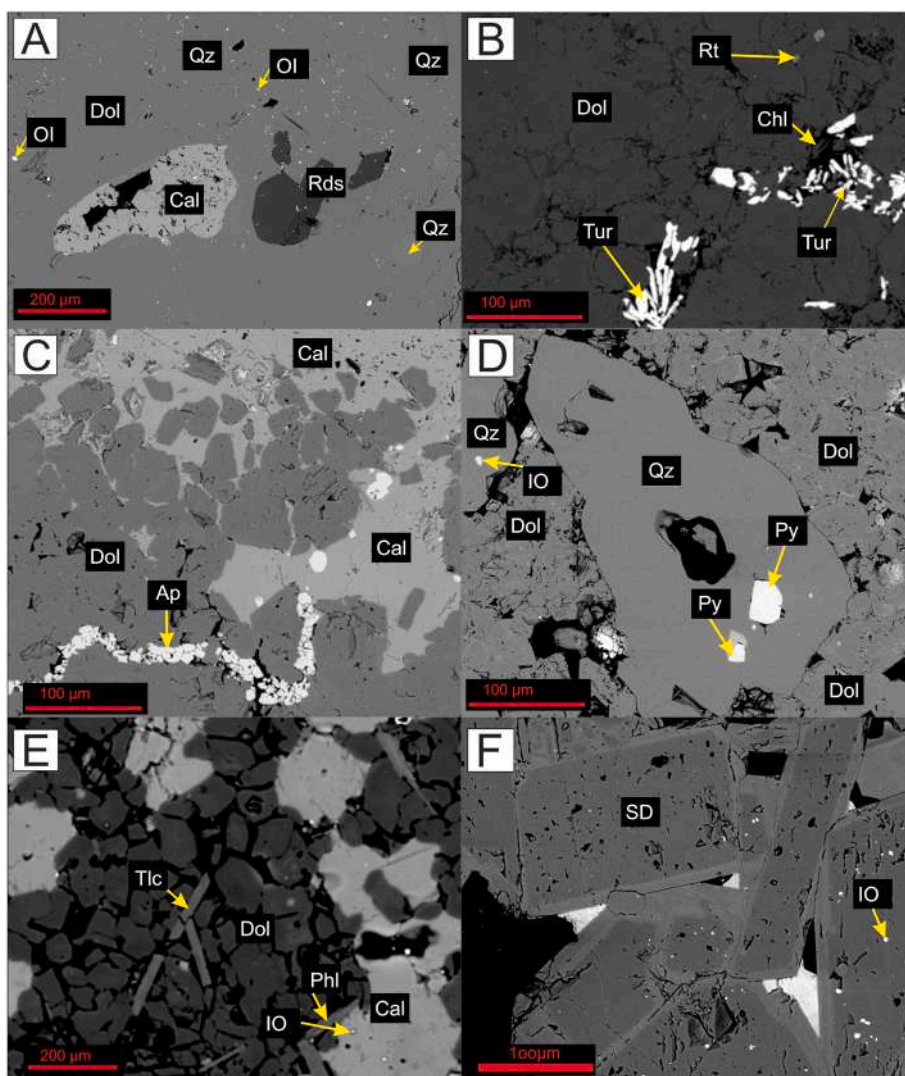


**Fig. 11.** Backscattered electron (BSE) images showing the mineralogical assemblages observed in the sample. **A.** Matrix predominantly composed of dolomite (Dol) and quartz (Qz), with inclusions of hematite (Hem) and rhodochrosite (Rds). **B.** Dolomite associated with rutile (Rt) and chlorite (Chl), along with needle-like formations of tourmaline (Tur). **C.** Coexistence of calcite (Cal) and apatite (Ap), with multiple occurrences of apatite within the calcite matrix. **D.** Pyrite (Py) inclusions within the quartz and dolomite framework. **E.** Talc (Tlc) and phlogopite (Phl) interspersed among the dolomite grains, indicating complex mineral interactions. **F.** Well-formed dolomite crystals with significant intergrowths.

largely overlap with those of the D1 and D2 and coeval seawater. This indicates that the dolomitizing fluids responsible for D3 were likely derived from mixture of contemporaneous seawater and hydrothermal fluids sourced from submarine felsic volcanism. The presence of relatively positive  $\delta^{18}\text{O}$  values suggests that the dolomitizing fluids experienced  $\delta^{18}\text{O}$  enrichment through extensive fluid-rock interactions (Tucker and Wright, 2009; Dong et al., 2017).

### 5.5. Origin of the CD

CD is typically observed in the fracture system, suggesting the migration of dolomitizing fluids is facilitated by fractures (Fig. 4E and 9D) (Warren and Kempton, 1997). The nonplanar s/e texture of CD1 suggests that it primarily precipitated at temperatures averaging 145.9 °C, exceeding the roughening threshold (Gregg and Sibley, 1984, 1987). This is further supported by the clumped isotope results. The fine to medium crystals and subhedral to euhedral textures indicate that CD formed slowly in  $\text{Mg}^{2+}$ -depleted fluids, which is observable in the zoning saddle dolomite (Fig. 10). Consequently, as  $\text{Mg}^{2+}$  got depleted, CD stopped precipitating, and hydrothermal activity led to late-stage

calcite fillings. The precipitation within the low temperature of calcite (average 36.7 °C) range confirms the last stage of mineralizing fluids. The transition from D3 to CD (Fig. 9) suggest that both D3 and CD precipitated from the same dolomitizing fluid at different stages. The undulatory extinctions and saddle-like or baroque crystal shapes of SD dolomite indicate its precipitation at high temperatures and pressure (Davies and Smith, 2006) that also got reflected in estimated temperature based on clumped isotopic results (average 150.3 °C). The  $\delta^{13}\text{C}$  (−3.88 to 1.73‰) and  $\delta^{18}\text{O}$  (−4.39 to −1.80‰) values of CD1 dolomite and  $\delta^{13}\text{C}$  (−6.32 to −0.55‰) and  $\delta^{18}\text{O}$  (−7.91 to −2.86‰) of SD overlap with other types of recrystallized dolomite (Table 2), indicating that CD formed from dolomitizing fluids similar to those that created other types of dolomite. Compared to SD (average 150.3 °C), the similar temperatures observed in CD1 (average 145.9 °C) suggest that the CD samples were formed from a consistent mixture of hydrothermal fluids and connate seawater during the final stages of hydrothermal activity. The hydrothermal alteration filling fractures in dolomite includes two main types: (i) CD1 to calcite, and (ii) CD1 to SD to calcite. These indicate changes in  $\text{Mg}^{2+}$  concentrations and fluid evolution stages. Dolomitization appears to be observed across various lithologies. Consequently, the

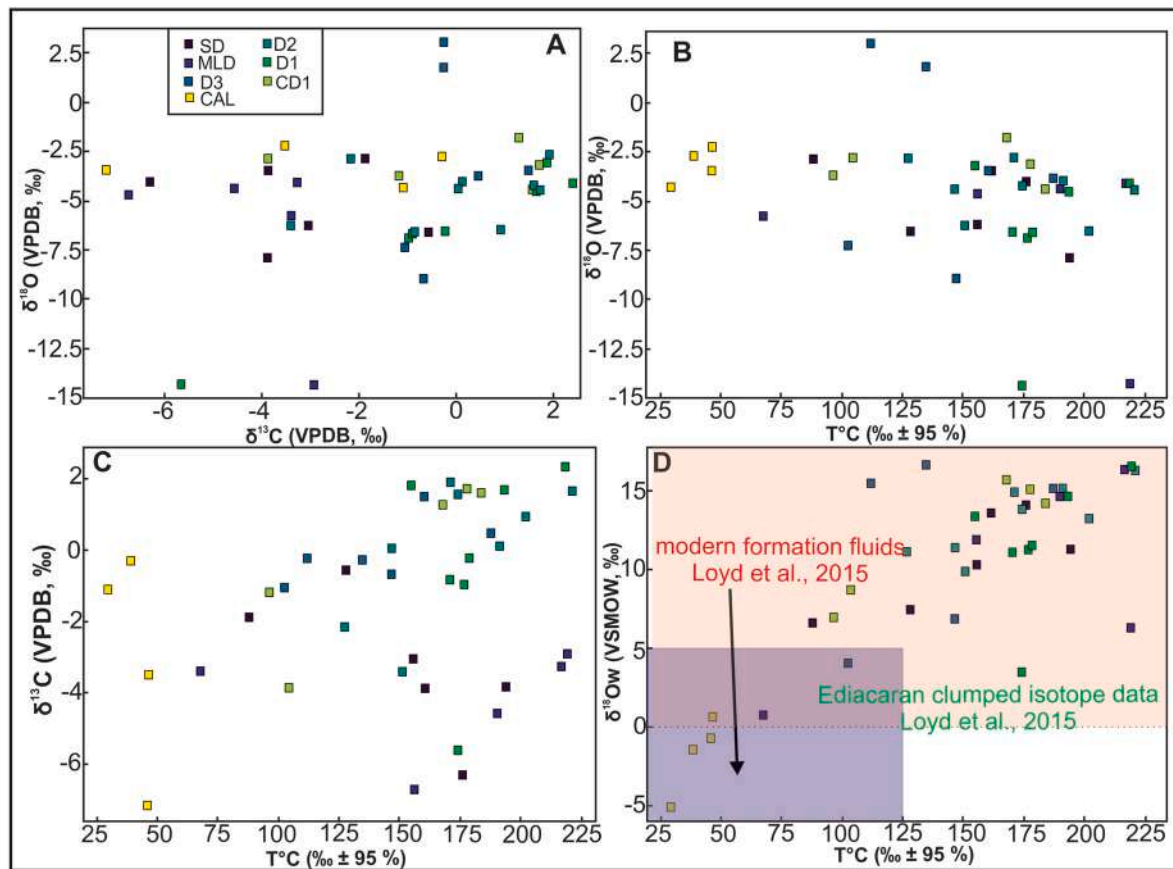


**Fig. 12.** Cross plot of isotopic analysis. A.  $\delta^{13}\text{C}_{\text{VPDB}}$  versus  $\delta^{18}\text{O}_{\text{VPDB}}$ . B.  $\Delta_{47}$  versus  $\delta^{18}\text{O}_{\text{VSMOW}}$ . C. Temperature ( $T$  °C) versus  $\delta^{13}\text{C}_{\text{VPDB}}$ . D. Temperature ( $T$  °C) versus Water  $\delta^{18}\text{O}_{\text{VSMOW}}$ .

hydrothermal alteration and the development of abundant CDs, followed by the precipitation of limited calcite within the fracture systems, suggest that the hot brine became depleted in  $\text{Mg}^{2+}$  (Allan and Wiggins, 1993; Wendte et al., 2009). A high degree of overlap with the  $\delta^{13}\text{C}$  and  $\delta^{18}\text{O}$  between hydrothermally altered dolomites and the previous dolomites (D1 and D2) and calcite suggests that hydrothermally altered dolomites not only inherited the original geochemical signatures but also originates from the surrounding rocks.

### 5.6. Origin of quartz & calcite

A close spatial association of quartz with SD and CD1 (Fig. 9A–C) suggests silica enrichment in hydrothermal fluids possibly derived from concurrent volcanic activities (Faramarzi et al., 2015; Asadi Sarshar et al., 2022). The transition from microcrystalline to granular dolomite filling fractures and porosity (Fig. 5D and 10D) suggests a hydrothermal fluid source of silica rather than a sedimentary origin. In addition, the maximum estimated temperature of CD (193.8 °C) supports an original hydrothermal origin. Hydrothermal fluids derived from volcanic activity became oversaturated with silica during the final stage, leading to the precipitation of siliceous minerals in the late phase (Plumlee et al., 1994; Dong et al., 2017).

Late calcite cements, which filled the fractures after the CD and D3, have a transitional contact with the CD (Fig. 10), indicating they were precipitated from the same diagenetic fluids. The precipitation temperature of the late calcite is 40.2 °C, indicating that it precipitated during the final stage of fluid activity as the fluids were cooling or seawater were caused precipitation of calcite at last stage. However,  $\delta^{18}\text{O}$  and  $\delta^{13}\text{C}$  values of late cement calcites, which mostly resemble with those of the CD, indicate that both late calcite and CD are derived from consistent hydrothermal fluids.

### 5.7. Implication of the late Ediacaran dolomitization

Our detail sedimentological and petrological observations reveal that dolomite occurrences and textures are diverse in the late Ediacaran cap carbonates of the Hormuz Complex. LMD samples preserve their original fabrics, with the dolomite crystals being smaller than 24  $\mu\text{m}$ . The temperature of these samples, typically <100 °C, often suggests the presence of primary dolomites, especially in the stromatolitic dolomite. The presence of stromatolitic dolomite could have promoted the development of extensive BSR or thermochemical sulfate reduction, which could have provided numerous nucleation sites for these primeval dolomites (seed crystals, Warren, 2000). However, a secondary origin of the dolomites may be considered for those that do not exhibit any fabric or were precipitated at temperatures >100 °C.

The overlap between  $\delta^{13}\text{C}$  and  $\delta^{18}\text{O}$  signature of LMD, MD and CD indicate that the original dolomitizing fluids were derived from the Mg-rich fluids with sub marine volcanic activities during late Ediacaran time (Fig. 13) (Faramarzi et al., 2015; Sharshar, 2022). Calcium was probably sourced from seawater,  $\text{CO}_3^{2-}$  from organic matter (stromatolites), and Mg-rich fluids from hydrothermal activities driven by volcanic processes or reflux of Mg-rich seawater (Warren, 2000; Gregg et al., 2015; Chang et al., 2020). The reaction between these components produced dolomites during the late Ediacaran Period as follows:



The subsequent cycling of hydrothermal fluids through primary dolomites resulted in metasomatism and dedolomitization. The occurrence of minerals such as phlogopite ( $(\text{KMg}_3(\text{AlSi}_3\text{O}_{10})(\text{OH})_2)$ ), tourmaline ( $(\text{Na,Ca})(\text{Mg,Fe,Li,Al})_3\text{Al}_6(\text{BO}_3)_3\text{Si}_6\text{O}_{18}(\text{OH,F})_4$ ), rutile ( $\text{TiO}_2$ ), and talc ( $\text{Mg}_3\text{Si}_4\text{O}_{10}(\text{OH})_2$ ) highlights that the source of the dolomitizing

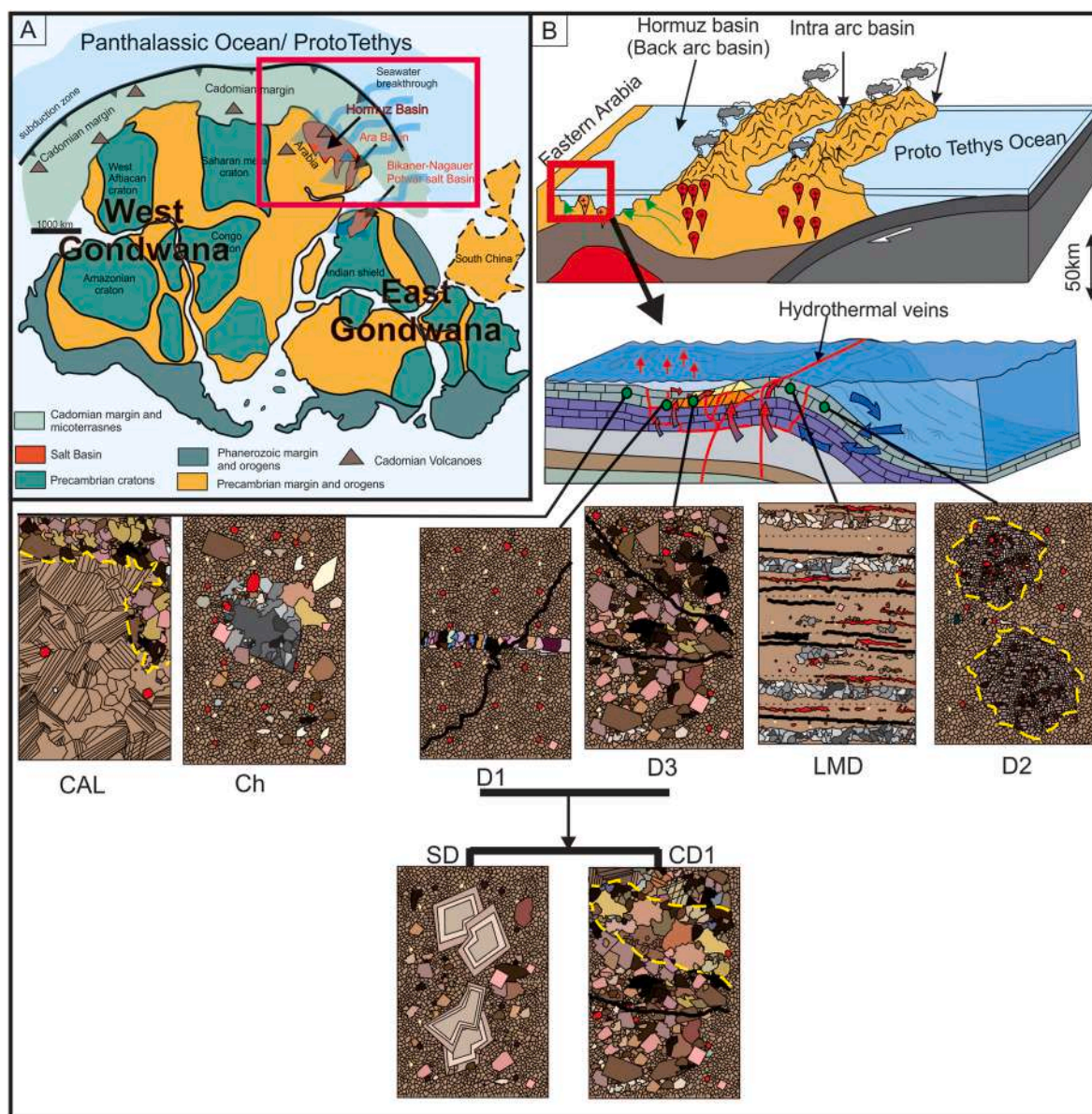


**Fig. 13.** A. location of the Hormuz basin during Late Ediacaran time (Modified after Stewart et al., 2020). B. Conceptual model for the development of the dolomite controlling by hydrothermal activities.

fluids was Mg-rich hydrothermal fluids sourced from cadomian volcanic activities (Asadi Sarshar et al., 2022). These high-temperature fluids metamorphosed the Late Ediacaran primary dolostones of the Hormuz Complex (Aftabi et al., 2022).

In hydrothermal systems, fluids interact with the dolomitic host rock, introducing various elements such as silica, iron, titanium, boron, sulfur, phosphorus, potassium, and manganese. These fluids, often heated by volcanic or metamorphic activity, cause the formation of new minerals or alter the existing dolomites. Metasomatism, dedolomitization and recrystallization are the key processes, leading to the complex assemblage of minerals e.g., quartz, rutile, tourmaline, chlorite, talc, phlogopite etc. within the dolomitic framework.

Lastly, the presence of low-amplitude stylolites is often seen as an indicator marking a shallow burial (Ronchi et al., 2011; Jacquemyn et al., 2014). This suggests that the salt diapirs sampled the dolomite and brought it to the surface, preventing evidence of a deep burial environment. Therefore, volcanism and associated hydrothermal fluids played a crucial role in the deposition of various dolomite types during the late Ediacaran to early Cambrian Period. Further investigation

would be required to understand the relationships between mineral assemblages in the dolomite samples, which will shed light on the complex interactions between volcanism, hydrothermal activity and dolomitization.

## 6. Conclusions

Based on petrographic, isotopic geochemistry (carbon, oxygen, and clumped isotopes), and SEM analyses, this study identifies laminated micritic dolomite, three types of matrix dolomites, and two types of dolomite cements in the late Ediacaran cap carbonates of the Hormuz Complex. The identified dolomites include: (i) very finely to finely crystalline planar-e/s dolomite with preserving fabrics (LMD); (ii) very finely to finely crystalline planar-e/s dolomite (D1); (iii) finely to medium crystalline planar-a/s dolomite (D2); and (iv) medium to coarsely crystalline nonplanar-a dolomite (D3). Additionally, two types of dolomite cements are found: (i) finely to medium crystalline nonplanar-s/e dolomites (CD1), and (ii) medium to coarsely crystalline nonplanar saddle dolomites (SD). Silica is another cement found alongside CD,

while calcite cement is the final fill within residual pores or fractures, indicating complex diagenetic processes.

The  $\delta^{13}\text{C}$  and  $\delta^{18}\text{O}$  values of the dolomites exhibit significant overlap, indicating that the dolomitizing fluids likely originated from similar sources, including recycled seawater and hydrothermal activity associated with volcanic processes. The dolomites display both low- and high-temperature formation characteristics, indicating multiple stages of dolomitization. Fluid evolution was influenced by variations in temperature, porosity, and hydrothermal conditions, resulting in a diverse range of crystal sizes and textures, which point to a complex, multi-stage precipitation process. The  $\text{Mg}^{2+}$ -depleted nature of the dolomitizing fluids, along with quartz and calcite precipitates, suggests a hydrothermal origin enriched in silica, likely sourced from volcanic activity. Following hydrothermal dolomitization, calcite cement extensively filled remaining fractures and pores at low temperature, marking the final stage of mineralization. The diversity in dolomite types, mineral assemblages, and isotopic signatures ( $\delta^{13}\text{C}$  and  $\delta^{18}\text{O}$ ) highlights the significant influence of Cadomian volcanism on dolomitization, with subsequent fluid-rock interactions preserving the original geochemical characteristics. Exhibiting negative  $\delta^{13}\text{C}$  values in the LMD likely formed during the late Ediacaran period suggests that hydrothermal fluids interacted with organic-rich sediments. The presence of pyrite in dolomite formations indicates the involvement of sulfate reduction processes during dolomitization. Overall, this study provides valuable insights into the evolution of dolomitizing fluids and their impact on the mineralogy and geochemistry of the Ediacaran cap carbonates in the Hormuz Basin during late Ediacaran time. These findings contribute to a broader understanding of dolomite formation under complex hydrothermal conditions and underscore the importance of volcanic influences on diagenetic processes.

#### CRedit authorship contribution statement

**Sadeh Adineh:** Writing – original draft, Visualization, Methodology, Investigation, Conceptualization. **Prokop Závada:** Supervision, Resources, Project administration, Investigation. **Soumyajit Mukherjee:** Writing – review & editing. **Jirí Bruthans:** Resources, Investigation, Formal analysis. **Mohammad Zare:** Resources, Project administration.

#### Declaration of Competing Interest

The authors declare that they have no known competing financial interests or personal relationships that could have appeared to influence the work reported in this paper.

#### Acknowledgements

This study was financially supported by and the Czech Science Foundation (GACR), Czechia No. 20–18647J and the Grantová agentura Univerzity Karlovy, Czechia (GAUK), Czechia with grant number 1542120. Ali Nokhbatolfoghahaei and Maryam Shahri contributed to fieldwork. Thanks to Martin Racek (Charles University in Prague, electron microprobe) and Discussions with Mathieu Daëron helped to shape the manuscript. Martin Racek (Charles University in Prague, electron microprobe) and Mathieu Daëron (aLaboratoire des Sciences du Climat et de l'Environnement, Université Paris-Saclay, France) Carbon, Oxygen and Clumped Isotopic measurements) are acknowledged for acquisition and processing of the compositional datasets. We thank editor Prof. Mirosław Slowakiewicz and anonymous reviewers for their comments that have improved this paper.

#### Appendix A. Supplementary data

Supplementary data to this article can be found online at <https://doi.org/10.1016/j.marpetgeo.2024.107228>.

#### Data availability

The authors do not have permission to share data.

#### References

- Adineh, S., Závada, P., Heuss-Aßbichler, S., Bruthans, J., Daëron, M., Petrash, D.A., 2023. Carbonate formation and alteration in the salt diapir caprock (Paskhand salt diapir, Southern Iran). In: EGU General Assembly Conference Abstracts. EGU-10828.
- Adineh, S., Závada, P., Bruthans, J., Cofrade, G., Zare, M., 2024. Growth of a salt diapir in an anticline-A record from the Cenozoic halokinetic sequences in the Zagros Fold and Thrust Belt, Iran. *J. Struct. Geol.* 178, 105004.
- Aftabi, A., Atapour, H., Mohseni, S., 2022. The Ediacaran record of glaciogenic dropstones, diamictites and cap carbonates associated with non-metamorphosed banded iron formations (BIFs) in Iran. *Precambrian Res.* 378, 106740.
- Al-Aasm, I.S., Abdallah, H., 2006. The origin of dolomite associated with salt diapirs in central Tunisia: preliminary investigations of field relationships and geochemistry. *J. Geochem. Explor.* 89 (1–3), 5–9.
- Allan, J.R., Wiggins, W.D., 1993. Dolomite reservoirs: Geochemical techniques for evaluating origin and distribution. American Association of Petroleum Geologists.
- Allen, P.A., 2007. The Huqf Supergroup of Oman: basin development and context for Neoproterozoic glaciation. *Earth Sci. Rev.* 84 (3–4), 139–185.
- Asadi Sarshar, M., Moghadam, H.S., Griffin, W.L., Santos, J.F., Stern, R.J., Ottley, C.J., Sarkarnejad, K., Sepidbar, F., O'Reilly, S.Y., 2022. Geochronology and geochemistry of exotic blocks of Cadomian crust from the salt diapirs of SE Zagros: the Chah-Banu example. *Int. Geol. Rev.* 64 (10), 1409–1430.
- Asl, M.E., Faghih, A., Mukherjee, S., Soleimany, B., 2019. Style and timing of salt movement in the Persian Gulf Basin, offshore Iran: insights from halokinetic sequences adjacent to the Tonb-e-Bozorg salt diapir. *J. Struct. Geol.* 122, 116–132.
- Aubert, N.R., Pecoits, E., Bekker, A., et al., 2012. Chemostratigraphic constraints on Early Ediacaran carbonate ramp dynamics, Rio de la Plata craton, Uruguay. *Gondwana Res.* 22, 1073–10890.
- Bahroudi, A., Koyi, H., 2003. Effect of spatial distribution of Hormuz salt on deformation style in the Zagros fold and thrust belt: an analogue modelling approach. *J. Geol. Soc.* 160 (5), 719–733.
- Bernasconi, S.M., Müller, I.A., Bergmann, K.D., Breitenbach, S.F., Fernandez, A., Hodel, D.A., Jaggi, M., Meckler, A.N., Millan, L., Ziegler, M., 2018. Reducing uncertainties in carbonate clumped isotope analysis through consistent carbonate-based standardization. *G-cubed* 19 (9), 2895–2914.
- Bernasconi, S.M., Daëron, M., Bergmann, K.D., Bonifacie, M., Meckler, A.N., Affek, H.P., Anderson, N., Bajnai, D., Barkan, E., Beverly, E., Blamart, D., 2021. InterCarb: a community effort to improve interlaboratory standardization of the carbonate clumped isotope thermometer using carbonate standardizations. *G-cubed* 22 (5), e2020GC009588.
- Bosák, P., Jaroš, J., Spudil, J., Sulovský, P., Vaclavěk, V., 1998. Salt plugs in the eastern Zagros, Iran: results of regional geological reconnaissance. *Geolines* 7 (1).
- Bowring, S.A., Grotzinger, J.P., Condon, D.J., Ramezani, J., Newall, M.J., Allen, P.A., 2007. Geochronologic constraints on the chronostratigraphic framework of the Neoproterozoic Huqf Supergroup, Sultanate of Oman. *Am. J. Sci.* 307 (10), 1097–1145.
- Braithwaite, C.J., Rizzi, G., Darke, G., 2004. The geometry and petrogenesis of dolomite hydrocarbon reservoirs: introduction. Geological Society, London, Special Publications 235 (1), 1–6.
- Brand, W.A., Assonov, S.S., Coplen, T.B., 2010. Correction for the 17O interference in  $\delta$  (13C) measurements when analyzing CO2 with stable isotope mass spectrometry (IUPAC Technical Report). *Pure Appl. Chem.* 82 (8), 1719–1733.
- Bristow, T.F., Bonifacie, M., Derkowski, A., Eiler, J.M., Grotzinger, J.P., 2011. A hydrothermal origin for isotopically anomalous cap dolostone cements from south China. *Nature* 474 (7349), 68–71.
- Caesar, K.H., Kyle, J.R., Lyons, T.W., Tripati, A., Loyd, S.J., 2019. Carbonate formation in salt dome cap rocks by microbial anaerobic oxidation of methane. *Nat. Commun.* 10 (1), 808.
- Cantine, M.D., Knoll, A.H., Bergmann, K.D., 2020. Carbonates before skeletons: a database approach. *Earth Sci. Rev.* 201, 103065.
- Chang, B., Li, C., Liu, D., Foster, I., Tripati, A., Lloyd, M.K., Maradiaga, I., Luo, G., An, Z., She, Z., Xie, S., 2020. Massive formation of early diagenetic dolomite in the Ediacaran ocean: constraints on the “dolomite problem”. *Proc. Natl. Acad. Sci. USA* 117 (25), 14005–14014.
- Chen, D., Qing, H., Yang, C., 2004. Multistage hydrothermal dolomites in the middle devonian (givetian) carbonates from the gulin area, south China. *Sedimentology* 51 (5), 1029–1051.
- Daëron, M., 2021. Full propagation of analytical uncertainties in  $\Delta 47$  measurements. *G-cubed* 22 (5), e2020GC009592.
- Daëron, M., Blamart, D., Peral, M., Affek, H.P., 2016. Absolute isotopic abundance ratios and the accuracy of  $\Delta 47$  measurements. *Chem. Geol.* 442, 83–96.
- Davies, G.R., Smith Jr., L.B., 2006. Structurally controlled hydrothermal dolomite reservoir facies: An overview. *AAPG Bull.* 90 (11), 1641–1690.
- Dong, S., Chen, D., Zhou, X., Qian, Y., Tian, M., Qing, H., 2017. Tectonically driven dolomitization of Cambrian to Lower Ordovician carbonates of the Qurugtagh area, north-eastern flank of Tarim Basin, north-west China. *Sedimentology* 64 (4), 1079–1106.
- Edgell, H.S., 1996. Salt tectonism in the Persian Gulf basin. *Geological Society* 100 (1), 129–151. London, Special Publications.

- Faghieh, A., Ezati-Asl, M., Mukherjee, S., Soleimany, B., 2019. Characterizing halokinesis and timing of salt movement in the Abu Musa salt diapir, Persian Gulf, offshore Iran. *Mar. Petrol. Geol.* 105, 338–352.
- Fang, Y., Hobbs, F., Yang, Y., Xu, H., 2023. Dissolved silica-driven dolomite precipitation in the Great Salt Lake, Utah, and its implication for dolomite formation environments. *Sedimentology* 70 (4), 1328–1347.
- Faramarzi, N.S., Amini, S., Schmitt, A.K., Hassanzadeh, J., Borg, G., McKeegan, K., Razavi, S.M.H., Mortazavi, S.M., 2015. Geochronology and geochemistry of rhyolites from Hormuz Island, southern Iran: a new record of Cadomian arc magmatism in the Hormuz Formation. *Lithos* 236, 203–211.
- Farzipour Saen, A., Valinejad, M., H., Motamedi, 2007. *Geological Map of Iran, 1: 100 000, Series Sheet 33-6844 BASTAK*.
- Ghazban, F., Al-Aasm, I.S., 2010. Hydrocarbon-induced diagenetic dolomite and pyrite formation associated with the Hormoz Island salt dome, offshore Iran. *J. Petrol. Geol.* 33 (2), 183–196.
- Gregg, J.M., 2004. Basin fluid flow, base-metal sulphide mineralization and the development of dolomite petroleum reservoirs. Geological Society, London, Special Publications 235 (1), 157–175.
- Gregg, J.M., Sibley, D.F., 1984. Epigenetic dolomitization and the origin of xenotopic dolomite texture. *J. Sediment. Res.* 54 (3), 908–931.
- Gregg, J.M., Bish, D.L., Kaczmarek, S.E., Machel, H.G., 2015. Mineralogy, nucleation and growth of dolomite in the laboratory and sedimentary environment: a review. *Sedimentology* 62 (6), 1749–1769.
- Guo, R., Zhang, S., Wang, K., Han, M., Ding, X., 2021. Multiphase dolomitization and hydrothermal alteration of the Upper Cambrian-Lower Ordovician carbonates in the Gucheng uplift, Tarim Basin (NW China). *J. Petrol. Sci. Eng.* 206, 108964.
- Hoffman, P.F., 2011. Strange bedfellows: glacial diamicrite and cap carbonate from the Marinoan (635 Ma) glaciation in Namibia. *Sedimentology* 58 (1), 57–119.
- Holland, H.D., Zimmermann, H., 2000. The dolomite problem Revisited. *Int. Geol. Rev.* 42 (6), 481–490.
- Jacquemyn, C., El Desouky, H., Hunt, D., Casini, G., Swennen, R., 2014. Dolomitization of the Latemar platform: fluid flow and dolomite evolution. *Mar. Petrol. Geol.* 55, 43–67.
- Jahani, S., Callot, J.P., de Lamotte, D.F., Letouzey, J., Leturmy, P., 2007. The salt diapirs of the eastern Fars Province (Zagros, Iran): A brief outline of their past and present. In: Thrust belts and foreland basins: From fold kinematics to hydrocarbon systems. Springer Berlin Heidelberg, pp. 289–308.
- Kaufman, A.J., Hayes, J.M., Knoll, A.H., Germs, G.J., 1991. Isotopic compositions of carbonates and organic carbon from upper Proterozoic successions in Namibia: stratigraphic variation and the effects of diagenesis and metamorphism. *Precamb. Res.* 49 (3–4), 301–327.
- Kent, P.E., 1958. Recent studies of south Persian salt plugs. *AAPG (Am. Assoc. Pet. Geol.) Bull.* 42 (12), 2951–2972.
- Kent, P.E., 1979. The emergent Hormuz salt plugs of southern Iran. *J. Petrol. Geol.* 2 (2), 117–144.
- Kernen, R.A., Giles, K.A., Poe, P.L., Gannaway Dalton, C.E., Rowan, M.G., Fiduc, J.C., Hearon, T.E., 2020. Origin of the Neoproterozoic rim dolomite as lateral carbonate caprock, Patawarta salt sheet, Flinders Ranges, South Australia. *Aust. J. Earth Sci.* 67 (6), 815–832.
- Kim, S.T., O'Neil, J.R., Hillaire-Marcel, C., Mucci, A., 2007. Oxygen isotope fractionation between synthetic aragonite and water: influence of temperature and Mg<sup>2+</sup> concentration. *Geochem. Cosmochim. Acta* 71 (19), 4704–4715.
- Liu, D., Xu, Y., Papineau, D., Yu, N., Fan, Q., Qiu, X., Wang, H., 2019. Experimental evidence for abiotic formation of low-temperature proto-dolomite facilitated by clay minerals. *Geochem. Cosmochim. Acta* 247, 83–95.
- Lloyd, S.J., Corsetti, F.A., Eagle, R.A., Hagadorn, J.W., Shen, Y., Zhang, X., Bonifacie, M., Tripati, A.K., 2015. Evolution of neoproterozoic wonoka-shuram anomalously-aged carbonates: evidence from clumped isotope paleothermometry. *Precambrian Res.* 264, 179–191.
- Machel, H.G., 2000. Application of cathodoluminescence to carbonate diagenesis. In: *Cathodoluminescence in Geosciences*, pp. 271–301. Berlin, Heidelberg: Springer Berlin Heidelberg.
- Machel, H.G. and Lonnee, J., 2002. Hydrothermal dolomite—A product of poor definition and imagination. *Sedimentary geology*, 152(3–4), pp.163–171.
- Machel, H.G., Cavell, P.A., 1999. Low-flux, tectonically-induced squeegee fluid flow (“hot flash”) into the Rocky Mountain Foreland Basin. *Bull. Can. Petrol. Geol.* 47 (4), 510–533.
- McKenzie, J.A., Vasconcelos, C., 2009. Dolomite Mountains and the origin of the dolomite rock of which they mainly consist: historical developments and new perspectives. *Sedimentology* 56 (1), 205–219.
- Mercollì, I., Briner, A.P., Frei, R., Schönberg, R., Nägler, T.F., Kramers, J., Peters, T., 2006. Lithostratigraphy and geochronology of the neoproterozoic crystalline basement of salalah, dhofar, sultanate of Oman. *Precambrian Res.* 145 (3–4), 182–206.
- Montes-Hernandez, G., Findling, N., Renard, F., 2016. Dissolution-precipitation reactions controlling fast formation of dolomite under hydrothermal conditions. *Appl. Geochem.* 73, 169–177.
- Moore, C.H., Wade, W.J., 2013. *Carbonate Reservoirs: Porosity and Diagenesis in a Sequence Stratigraphic Framework*. Elsevier, Amsterdam. Dev. Sediment. 374.
- Mortazavi, M., Heuss-Assbichler, S., Shahri, M., 2017. Hydrothermal systems in the salt domes of south Iran. *Procedia Earth and Planetary Science* 17, 913–916.
- Motamedi, H., Sepehr, M., Sherkati, S., Pourkermani, M., 2011. Multi-phase Hormuz salt diapirism in the southern Zagros, SW Iran. *J. Petrol. Geol.* 34 (1), 29–43.
- Mukherjee, S., Talbot, C.J., Koyi, H.A., 2010. Viscosity estimates of salt in the Hormuz and Namakdan salt diapirs, Persian Gulf. *Geol. Mag.* 147, 497–507.
- Nasir, S., Al-Saad, H., Alsayigh, A., Weidlich, O., 2008. Geology and petrology of the Hormuz dolomite, infra-cambrian: implications for the formation of the salt-cored halul and shraouh islands, offshore, state of Qatar. *J. Asian Earth Sci.* 33, 353–365.
- Nokhbatolfighahaei, A., Nezafati, N., Ghorbani, M., Abdolabadi, B.E., 2019. Evidence for origin and alteration in the dolomites of salt diapirs, Larestan, Southern Iran. *Carbonates Evaporites* 34, 389–403.
- Perona, J., Canals, A., Cardellach, E., 2018. Zn-Pb mineralization associated with salt diapirs in the Basque-Cantabrian Basin, northern Spain: geology, geochemistry, and genetic model. *Econ. Geol.* 113 (5), 1133–1159.
- Plumlee, G.S., Leach, D.L., Hofstra, A.H., Landis, G.P., Rowan, E.L., Viets, J.G., 1994. Chemical reaction path modeling of ore deposition in Mississippi Valley-type Pb-Zn deposits of the Ozark region, US Midcontinent. *Econ. Geol.* 89 (6), 1361–1383.
- Poe, P., Kernen, R., Giles, K., Brunner, B., Labrado, A., Lerer, K., 2018. New Classification of Caprock Associated with Salt Diapirs.
- Posey, H.H., Kyle, J.R., Jackson, T.J., Hurst, S.D., Price, P.E., 1987. Multiple fluid components of salt diapirs and salt dome cap rocks, Gulf Coast, USA. *Appl. Geochem.* 2 (5–6), 523–534.
- Qing, H., Mountjoy, E.W., 1989. Multistage dolomitization in rainbow buildups, middle devonian keg river formation, Alberta, Canada. *J. Sediment. Res.* 59 (1), 114–126.
- Qing, H., Mountjoy, E.W., 1994. Formation of coarsely crystalline, hydrothermal dolomite reservoirs in the Presqu'île Barrier, Western Canada Sedimentary Basin. *AAPG Bull.* 78 (1), 55–77.
- Ramezani, J., Tucker, R.D., 2003. The Saghand region, central Iran: U-Pb geochronology, petrogenesis and implications for Gondwana tectonics. *Am. J. Sci.* 303 (7), 622–665.
- Ronchi, P., Jadoul, F., Ceriani, A., Di Giulio, A., Scotti, P., Ortenzi, A., Previde Massara, E., 2011. Multistage dolomitization and distribution of dolomitized bodies in Early Jurassic carbonate platforms (Southern Alps, Italy). *Sedimentology* 58 (2), 532–565.
- Rooney, A.D., Cantine, M.D., Bergmann, K.D., Gómez-Pérez, I., Al Baloushi, B., Boag, T. H., Busch, J.F., Sperling, E.A., Strauss, J.V., 2020. Calibrating the coevolution of Ediacaran life and environment. *Proc. Natl. Acad. Sci. USA* 117 (29), 16824–16830.
- Schmoker, J.W., Halley, R.B., 1982. Carbonate porosity versus depth: a predictable relation for south Florida. *AAPG Bull.* 66 (12), 2561–2570.
- Sibley, D.F., Gregg, J.M., 1987. Classification of dolomite rock textures. *J. Sediment. Res.* 57 (6), 967–975.
- Smith, A.G., 2012. A review of the Ediacaran to Early Cambrian (“Infra-Cambrian”) evaporites and associated sediments of the Middle East. Geological Society, London, Special Publications 366 (1), 229–250.
- Stern, R.J., Johnson, P., 2010. Continental lithosphere of the Arabian Plate: a geologic, petrologic, and geophysical synthesis. *Earth Sci. Rev.* 101 (1–2), 29–67.
- Stewart, S.A., 2020. Structural style of buried Ediacaran basins in Saudi Arabia on seismic reflection data. *Precambrian Res.* 351, 105954.
- Taghipour, S., Khalili, M., Mackizadeh, M.A., Kananian, A., Taghipour, B., 2013. Mineralogy, geochemistry and petrogenesis of igneous inclusions within three inactive diapirs, Zagros belt, Shahre-kord, Iran. *Geol. Mag.* 150 (1), 72–88.
- Thomas, R.J., Ellison, R.A., Goodenough, K.M., Roberts, N.M., Allen, P.A., 2015. Salt domes of the UAE and Oman: probing eastern Arabia. *Precambrian Res.* 256, 1–16.
- Tucker, M.E., Wright, V.P., 2009. *Carbonate Sedimentology*. John Wiley & Sons.
- Wang, R., Xing, C., Wen, B., Wang, X., Liu, K., Huang, T., Zhou, C., Shen, B., 2023a. The origin of cap carbonate after the Ediacaran glaciations. *Global Planet. Change* 226, 104141.
- Wang, R., Yin, Z., Shen, B., 2023b. A late Ediacaran ice age: the key node in the Earth system evolution. *Earth Sci. Rev.*, 104610.
- Warren, J., 2000. Dolomite: occurrence, evolution and economically important associations. *Earth Sci. Rev.* 52 (1–3), 1–81.
- Warren, J.K., Kempton, R.H., 1997. Evaporite sedimentology and the origin of evaporite-associated Mississippi Valley-type sulfides in the Cadjebut mine area, Lennard shelf, Canning basin, Western Australia.
- Warthmann, R., Van Lith, Y., Vasconcelos, C., McKenzie, J.A., Karpoff, A.M., 2000. Bacterially induced dolomite precipitation in anoxic culture experiments. *Geology* 28 (12), 1091–1094.
- Wendte, J., Chi, G., Al-Aasm, I., Sargent, D., 2009. Fault/fracture controlled hydrothermal dolomitization and associated diagenesis of the upper devonian jean marie member (redknife formation) in the July lake area of northeastern British Columbia. *Bull. Can. Petrol. Geol.* 57 (3), 275–322.
- Wood, R.A., Zhuravlev, A.Y., Sukhov, S.S., Zhu, M.Y., Zhao, F.C., 2017. Demise of Ediacaran dolomitic seas marks widespread biomineralization on the Siberian Platform. *Geology* 45 (1), 27–30.
- Yang, X., Tang, H., Wang, X., Wang, Y., Yang, Y., 2017. Dolomitization by penesaline sea water in early cambrian longwangmiao formation, central sichuan basin, China. *Journal of Earth Science* 28, 305–314.
- Závada, P., Bruthans, J., Adineh, S., Warsitzka, M., Zare, M., 2021. Composition and deformation patterns of the caprock on salt extrusions in southern Iran—Field study on the Karmostaj and Siah Taq diapirs. *J. Struct. Geol.* 151, 104422.
- Zhang, K., Liu, Z., Xu, Z., Chang, Q., Fathy, D., Liu, R., Bai, E., 2024. Microbial and hydrothermal dolomite formation in Early Cretaceous lacustrine sediments in Yin'e Basin: Insights from petrology and geochemistry. *Sediment. Geol.* 471, 106739.
- Zhou, C., Xiao, S., Wang, W., Guan, C., Ouyang, Q., and Chen, Z., 2017. The stratigraphic complexity of the middle Ediacaran carbon isotopic record in the Yangtze Gorges area, South China, and its implications for the age and chemostratigraphic significance of the Shuram excursion. *Precambrian Res.* 288, 23–38.